Title

Dynamics of upstream ESCRT organization at the HIV-1 budding site

Journal

Biophysical Journal, 122(13)

ISSN

0006-3495

Authors

Hudait, Arpa

Hurley, James H

Voth, Gregory A

Publication Date

2023-07-01

DOI

10.1016/j.bpj.2023.05.020

Peer reviewed

Biophysical Journal
Article

Biophysical Society

Dynamics of upstream ESCRT organization at the HIV-1 budding site

Arpa Hudait,[1] James H. Hurley,[2,3] and Gregory A. Voth[1,*]
[1]Department of Chemistry, Chicago Center for Theoretical Chemistry, Institute for Biophysical Dynamics, and James Franck Institute, The University of Chicago, Chicago, Illinois; [2]Department of Molecular and Cell Biology and California Institute for Quantitative Biosciences, University of California, Berkeley, Berkeley, California; and [3]California Institute for Quantitative Biosciences, University of California, Berkeley, Berkeley, California

ABSTRACT In the late stages of the HIV-1 life cycle, membrane localization and self-assembly of Gag polyproteins induce membrane deformation and budding. Release of the virion requires direct interaction between immature Gag lattice and upstream ESCRT machinery at the viral budding site, followed by assembly of downstream ESCRT-III factors, culminating in membrane scission. However, molecular details of upstream ESCRT assembly dynamics at the viral budding site remain unclear. In this work, using coarse-grained (CG) molecular dynamics (MD) simulations, we investigated the interactions between Gag, ESCRT-I, ESCRT-II, and membrane to delineate the dynamical mechanisms by which upstream ESCRTs assemble templated by late-stage immature Gag lattice. We first systematically derived "bottom-up" CG molecular models and interactions of upstream ESCRT proteins from experimental structural data and extensive all-atom MD simulations. Using these molecular models, we performed CG MD simulations of ESCRT-I oligomerization and ESCRT-I/II supercomplex formation at the neck of the budding virion. Our simulations demonstrate that ESCRT-I can effectively oligomerize to higher-order complexes templated by the immature Gag lattice both in the absence of ESCRT-II and when multiple copies of ESCRT-II are localized at the bud neck. The ESCRT-I/II supercomplexes formed in our simulations exhibit predominantly columnar structures, which has important implications for the nucleation pathway of downstream ESCRT-III polymers. Importantly, ESCRT-I/II supercomplexes bound to Gag initiate membrane neck constriction by pulling the inner edge of the bud neck closer to the ESCRT-I headpiece ring. Our findings serve to elucidate a network of interactions between upstream ESCRT machinery, immature Gag lattice, and membrane neck that regulate protein assembly dynamics at the HIV-1 budding site.

SIGNIFICANCE The budding of immature HIV-1 virions requires the recruitment of upstream ESCRT machinery at the late stages of viral protein assembly, which then recruit downstream ESCRT factors leading to membrane scission. Here, using coarse-grained simulations, we elucidate the network of interactions that regulate the structure and dynamics of upstream ESCRT organization at the viral budding site. We find that upstream ESCRT complexes form neck-scaffolding columnar structures in which the ESCRT-III binding regions of ESCRT-II are predominantly distributed at the outer periphery of the bud neck. Therefore, the ESCRT-III polymers are likely to be nucleated from the region of the neck distal to the immature Gag lattice. Our findings provide key molecular insights into how upstream ESCRT machinery primes the HIV-1 budding site for ESCRT-III nucleation.

INTRODUCTION

A critical step in the HIV-1 life cycle is the assembly of viral Gag polyproteins at the cellular membrane, followed by a series of membrane-remodeling events at the site of viral protein localization that culminates in budding and fission of the immature virion (1–4). To aid in viral particle release, HIV-1 recruits endosomal sorting complexes required for transport (ESCRT) machinery (5–8). Multiple studies have demonstrated significant inhibition of viral particle production when immature virions are unable to recruit the ESCRT machinery (9–12). ESCRT machinery facilitates membrane scission in a variety of other cellular processes, such as the formation of multivesicular bodies (13), nuclear envelope reformation (14), and cytokinetic membrane scission (15). ESCRTs predominantly direct budding and scission of membrane neck pointing away (reverse topology) from the cytoplasm. Recent studies have shown that ESCRT

Submitted December 9, 2022, and accepted for publication May 11, 2023.
*Correspondence: gavoth@uchicago.edu
Editor: Rumiana Dimova.
https://doi.org/10.1016/j.bpj.2023.05.020

complexes can also facilitate regular-topology scission (16–18), thus demonstrating versatility in their mechanism of action.

The initial events of immature virion formation involve steady recruitment of HIV-1 structural protein Gag at the plasma membrane (5,19). The matrix (MA) domain of the Gag polyprotein mediates interaction with the plasma membrane (20,21). The capsid (CA) and spacer peptide 1 (SP1) domains of Gag provide key protein-protein contacts for the assembly of a hexameric bundle, the building block of immature Gag lattice (22–24). Nucleation and growth of Gag lattice result in a quasi-spherical-shaped immature virion (25–27). Recruitment of ESCRT proteins at the viral assembly site closely follows Gag accumulation and oligomerization events (5,19,28). Gag polyproteins recruit ESCRT machinery through motifs in the C-terminal p6 domain that point inward to the center of the spherical shell. Specifically, the PTAP motif interacts with the ubiquitin E2 variant (UEV) domain of the ESCRT-I complex (10–12,29–31), and the $LYPX_nL$ motif interacts with ALG-2-interacting protein X (ALIX) (32–35). When bound to the Gag lattice, the headpiece region of ESCRT-I oligomerizes to a 12-membered ring facilitated by electrostatic interactions from residues in the VPS28 N-terminal domain (36). ESCRT-I binds to ESCRT-II, a peripheral membrane-targeting complex through the VPS28 C-terminal domain (CTD) in the headpiece region (37,38). Next, VPS25 subunits of ESCRT-II recruit CHMP6, the most upstream component of the ESCRT-III family, also a membrane-targeting protein (39,40). Overall, ESCRT-I, ESCRT-II, and ALIX constitute the upstream ESCRT machinery. ESCRT-I/II with CHMP6 provides one pathway for ESCRT-III nucleation and polymerization, while ALIX offers a secondary pathway by directly binding to ESCRT-III components leading to virion budding (28,41–44). It is well established that upstream ESCRTs play an essential role in regulating the downstream ESCRT-III self-assembly (Fig. S1).

Membrane-protein interactions and membrane-remodeling events are central to immature virion assembly, budding, and release. HIV-1 structural protein Gag binds to the membrane through a PIP2-targeting highly basic region and is anchored to membrane leaflet through the insertion of N-terminal myristoyl moiety (21,45). Early stages of Gag localization and hexamer nucleation can generate PIP2 and cholesterol-enriched nanodomains in the vicinity and spontaneous membrane curvature, which in turn can localize more Gag proteins and facilitate immature lattice growth (46–48). Upstream ESCRT-I, ESCRT-II, and CHMP6 are recruited to the budding site as the immature Gag lattice grows to a spherical shell (28). ESCRT-II is a peripheral membrane protein complex consisting of two membrane-targeting sites: a highly basic α-helix motif and a phosphatidylinositol lipid targeting the GLUE domain (37). CHMP6 association with the membrane is mediated by the N-terminal basic region and myristoyl anchoring (40). Further downstream, ESCRT-III associates with the membrane and self-assembles to filaments adopting multiple shapes such as spirals, helical tubes, and cones (49–53). Theoretical studies have proposed that membrane neck scission is caused by constricting forces exerted by the shape transition of ESCRT-III polymers coating the bud neck (54,55). At the bud neck, upstream ESCRT machinery bridges immature Gag lattices and downstream ESCRT-III components. How upstream ESCRTs sense local curvature to localize at the bud neck and influence bud neck shape remains an open question. Previous experimental and theoretical studies have reported that upstream ESCRTs can induce membrane deformation by localizing at the membrane neck in large concentrations facilitating vesicle formation (13,56,57). Other studies using analytical theory and continuum models demonstrated that upstream ESCRT complexes could generate spontaneous membrane curvature and budding (58,59).

We have previously shown, using coarse-grained (CG) molecular dynamics (MD) simulations, that ESCRT-I oligomerization is facilitated by optimal geometry of the immature Gag lattice (36). In this "geometry-dependent checkpoint" mechanism, higher-order ESCRT-I oligomers are formed at the late stages of Gag assembly. Specifically, we simulated ESCRT-I oligomerization for Gag shells of aperture diameters 47, 54, 63, and 75 nm. We found that higher-order ESCRT-I oligomers formed more efficiently for Gag shells of diameter 54 and 63 nm. As stated earlier, in addition to ESCRT-I, the upstream ESCRT machinery also consist of the membrane targeting the ESCRT-II complex. The membrane neck of a budding immature virion presents a heterogeneous, crowded, and confined environment where the structure of ESCRT-I/II supercomplexes is expected to be regulated by a complex network of interactions between Gag, ESCRT-I, ESCRT-II, and membrane. Experimental structural determination of ESCRT-I/II supercomplexes in a complex lipid environment mimicking the viral budding site remains challenging. Therefore, the primary motivation of this study is to provide a composite molecular model of the upstream ESCRT (-I and -II) organization at the interface of immature Gag lattice and bud neck. Specifically, how localization of ESCRT-II at the bud neck influences the dynamics of ESCRT-I assembly templated by an immature Gag lattice, the number of copies of ESCRT-I/II supercomplexes that spontaneously form at the bud neck of dimension relevant to late-stage immature virion, and the structure of ESCRT-I/II supercomplexes at the bud neck are open questions in the context of upstream ESCRT organization at viral budding sites. A detailed understanding of upstream ESCRT organization is also essential to elucidate the mechanism of downstream ESCRT-III nucleation and growth into membrane-remodeling polymers. The CG MD simulations are particularly effective in accessing the relevant lengths and timescales required to meaningfully simulate the dynamics of multiprotein

assembly and membrane remodeling (36,60), as opposed to MD simulations performed in atomistic detail, which are significantly more computationally demanding for the processes relevant for this work.

In this work, we utilize CG MD simulations to probe the dynamics of ESCRT-I assembly and ESCRT-II recruitment templated by an immature Gag lattice to shed light on the interactions regulating upstream ESCRT organization at the budding virion neck. We first performed all-atom (AA) MD simulations to characterize the specific interactions that regulate the association of full-length ESCRT-II protein with membrane and ESCRT-I. We then derived "bottom-up" CG molecular model and interactions of ESCRT-II in addition to the ESCRT-I and Gag CG models developed previously (36), allowing us to simulate the full upstream ESCRT machinery with the immature virion. Here, the term bottom-up means that the CG models are systematically derived from the underlying atomistic-level interactions, as opposed to developed in an ad hoc, "top-down" fashion (61). Using these CG molecular models, we simulated ESCRT-I oligomerization templated by the optimal Gag lattice aperture dimension of 50 nm. Specifically, we focus on how the presence of ESCRT-II at the bud neck modulates ESCRT-I oligomerization dynamics. Our results demonstrate that ESCRT-I remains assembly competent even when ESCRT-II crowds the bud neck and spontaneously forms ESCRT-I/II supercomplexes during the assembly process. ESCRT-I/II supercomplexes observed in our simulations predominantly exhibit structures resembling columns along the bud neck, therefore positioning the ESCRT-III nucleating domain of VPS25 subunits of ESCRT-II distal to the Gag-ESCRT-I scaffold. Our analysis reveals that ESCRT-I/II supercomplexes constrict the bud neck by pulling the neck closer to the ESCRT-I headpiece ring. Taken together, these observations provide insight into the molecular-scale mechanisms that regulate upstream ESCRT assembly at the budding virion and that initiate membrane remodeling.

MATERIALS AND METHODS

Atomic-level protein models

The initial atomic model for the full-length ESCRT-II complex was constructed by combining the crystallographic fragments of the VPS22: VPS36 complex (PDB: 3CUQ, 2ZME), VPS25 (PDB: 3CUQ, 2ZME), and GLUE domain (PDB: 2HTH) (37,62). The missing N-terminal α-helix (VPS22: 1–33) and the linker (VPS36: 132–171) connecting the C-terminal region of the GLUE domain and VPS36 core were constructed using the amino acid sequence from the Robetta server (63,64).

AA MD simulations

The membrane model used in this study to investigate the conformational state of membrane-bound ESCRT-II was composed of 76% POPC, 20% POPE, and 4% PIP2, based on the experimental study of ESCRT-II membrane binding (37). Two symmetric membrane models of the above-mentioned composition of dimension $17.2 \times 17.2\,nm^2$ and $9.5 \times 9.5\,nm^2$ were built to study membrane binding of ESCRT-II complex and monomeric membrane-targeting domains, respectively. The smaller lipid bilayer system was used to perform umbrella sampling (US)-enhanced free energy simulations. The model membranes were created and solvated using CHARMM-GUI Membrane Builder (65). The solvated bilayers were minimized, relaxed using the standard six-step protocol provided on CHARMM-GUI for a cumulative 750 ps, and then equilibrated for an additional 200 ns. The coordinates of the lipid molecules were then extracted from the final configuration of the equilibrated trajectories and merged with the protein coordinates. The ESCRT-II complex was oriented such that, in the initial configuration, the highly basic VPS22-H0 helix was 1 nm away from the membrane surface, and the H0-helix was coplanar to the membrane surface. The composite membrane-protein system was then equilibrated by applying harmonic positional restraints (spring constant value of 239 kcal/mol/nm^2) on protein and lipid heavy atoms for 500 ps, followed by another 500 ps of equilibration by harmonic restraints on only the protein C_a atoms. A further 300 ps of restrained equilibration was performed, and configurations were saved every 100 ps to be used as initial structures for independent production runs. The restrained simulations were performed with a constant NVT ensemble. The temperature of the system was maintained at 310 K using stochastic velocity rescaling the thermostat with a time constant of 1 ps. Production runs were carried out for 2000 ns in a constant NPT ensemble at 310 K and 1 bar. The temperature was maintained using a Nose-Hoover chain thermostat with a 2 ps time constant, and pressure with a semi-isotropic (x and y directions coupled) Parrinello-Rahman barostat with a 10 ps time constant (66,67). Identical setup protocol was used to build and equilibrate the protein-membrane system of the monomeric GLUE domain (VPS36: 1–132) and $VPS22_{Mem}$ (VPS22: 1–76) for the US simulations, and VPS28-CTD docked to VPS22:VPS36 subcomplex to derive the ESCRT-I/II CG attractive interactions.

All simulations were performed with periodic boundary conditions in x, y, and z directions, and timestep of 2 fs. The protein and lipid were modeled with CHARMM36m force field (68), and water was modeled with TIP3P parameters (69). LINCS algorithm was used to constrain the bonds between heavy and hydrogen atoms (70). Electrostatic interactions were computed using the particle mesh Ewald method with a cutoff of 1 nm (71), and van der Waals force was truncated smoothly to zero between 1.0 and 1.2 nm. All simulations were performed using the Gromacs 2019 package (72).

AA MD US simulations

We performed US simulations to estimate the free energy of binding to the membrane for the monomeric GLUE domain and $VPS22_{Mem}$. The distance between the z component of the center of mass of membrane bilayer and protein was used as the reaction coordinate for the US simulations. To generate configurations for US simulation windows, we performed steered molecular dynamics (SMD) simulations for each system. The initial configuration for the SMD simulations corresponds to the equilibrated structure at the end of the 200 ns production run for each system. In each case, the protein was pulled from the equilibrated bound state to the unbound state (6 nm from the membrane center). SMD simulations were performed with a constant pulling velocity of 10^{-4} nm ps^{-1} and configurations were saved every 0.05 nm to be used as starting configuration for US windows. We note that in the SMD simulations a 1 fs timestep is used. In the SMD simulations, harmonic positional restraints (spring constant value of 239 kcal/mol/nm^2) were applied to the lipid heavy atoms to prevent upward lipid displacement. For the US simulations, constrained simulation at each umbrella window was performed with 1000 kcal/mol/nm^2 harmonic force constant. For each protein, a total of 42 US windows was used to compute the potential of mean force (PMF) profile. Each umbrella window was evolved for 100 ns, resulting in a cumulative simulation time of 8400 ns. The PMF profile was computed from the last 75 ns of each US window using the weighted histogram analysis method (73,74). The statistical uncertainty of the PMF was evaluated using the block averaging method by dividing the data into five blocks of 15 ns each, and the PMF was calculated for each block (75). The standard deviation of the PMF was calculated from

the five PMFs corresponding to each block. The histogram showing the overlap between consecutive umbrella windows is shown in Fig. S5.

CG model generation of ESCRT-II

We derived a bottom-up model of ESCRT-II from the AA MD trajectories of the ESCRT-II bound to the membrane. The CG sites are mapped from the atomistic trajectories using the essential dynamics coarse-graining (EDCG) method (76). In the EDCG method, contiguous C_α atoms of the protein were grouped to CG sites to reflect the atomistic collective fluctuations, specifically the motions in the essential subspace determined from principal-component analysis of the reference AA trajectories. The resulting CG model of the ESCRT-II has 222 sites: the VPS22 and VPS36 subunit have 54 and 94 CG sites, respectively, and the two VPS25 subunits have 37 sites each. After defining the CG mapping, intramolecular interactions between the CG sites were represented as a network of effective harmonic bonds between a central CG site and all other CG sites within 3 nm. The force constants of the harmonic bonds are derived using the hetero-elastic network model (hENM) method (77). We validated the choice of hENM cutoff by comparing the root mean-square fluctuation of the CG ESCRT-II and mapped the AA trajectory. We found that 3 nm cutoff was the lowest value that yielded good agreement between hENM and AA fluctuations. Intermolecular CG interactions between proteins were modeled using a combination of excluded volume (E_{excl}) to avoid unphysical overlap between CG beads and attractive interactions (E_{attr}) between ESCRT-I and ESCRT-II. For E_{excl}, a soft cosine potential, $A\left(1+\cos\left(\frac{\pi r_{ij}}{r_c}\right)\right)$ is used, r_{ij} is the pairwise distance between CG site types i and j. The value of A is 25 kcal/mol for all ij pairs. The distance cutoff (r_c) between excluded volume interactions was set at 2.5 nm. Attractive interactions (E_{attr}) were modeled as a pairwise Gaussian potential, $\frac{H_{ij}}{\sigma_{ij}\sqrt{2\pi}}\exp\left(-\frac{(r_{ij}-r_{0,ij})^2}{2\sigma_{ij}^2}\right)$. Here, $r_{0,ij}$ and σ_{ij} are the mean and standard deviation of the distance between CG site types i and j determined by fitting to the corresponding pair correlation through least-squares regression. Here, σ_{ij} also represents the width of the potential well for a specific ij pair. All pair potentials used a 2.5 nm radial cutoff, except for the attractive interactions to drive ESCRT-I oligomerization, where a 3 nm radial cutoff was used.

CG model of lipids

In our simulations, we use a highly CG three-site lipid model. The nonbonded interactions between the lipids are modeled with custom soft pair potentials listed in (78). The three-site CG model is highly computationally efficient and is ideal for large-scale simulations with multiple membrane binding proteins.

CG interaction between ESCRT-I and ESCRT-II

The attractive pairwise interaction between VPS28-CTD of ESCRT-I and ESCRT-II was derived from an AA MD simulation trajectory of VPS28-CTD complexed to a membrane-bound VPS22:VPS36 subcomplex. The last 500 ns of this trajectory was used to map the C_α atoms to corresponding CG sites. For the VPS22:VPS36 subcomplex identical mapping is used as in the full-length ESCRT-II complex described previously. For the VPS28-CTD CG sites are mapped using the EDCG method with an average resolution of ~8 amino acid residues per CG site (76). The CG mapping resolution is consistent with the CG model of ESCRT-I headpiece, UEV domain, and stalk as in our previous CG study (36). From the CG mapped trajectory of VPS28-CTD complexed to a membrane bound VPS22:VPS36 subcomplex, we identified CG sites of VPS28-CTD (i) within 2 nm of any CG sites (j) of the VPS22-VPS36 subcomplex, and with a standard deviation lower than 0.18 nm. These CG site pairs (ij) are assumed to be in close contact and hence contribute toward ESCRT-I/II association. The coefficient H_{ij} of these CG pair sites was optimized through the relative entropy minimization (REM) method (79). A detailed description of the REM method to derive the CG attractive interprotein interactions from AA MD trajectories is provided in (80,81), where REM was used to optimize attractive interactions between SARS-CoV-2 structural proteins. In brief, in REM we optimize H_{ij} using the iterative Newton-Raphson method. Different initial H_{ij} values were initially chosen and, at the end of the learning cycle, we compared the pair correlation function of the selected CG sites (ij) for H_{ij} values. A total of 500 step iteration cycles was performed as changes between successive steps were effectively zero within 500 steps. Learning rate (χ) was varied as 0.5 (1–100 steps), 0.1 (101–200 steps), and 0.01 (201–500 steps). Using REM, we obtained an optimized H_{ij} value of −0.8 nm kcal/mol. In the results, we denote the AA-derived CG energy interaction as $E_{\mathrm{Esc\text{-}I/II}}$ ($=\frac{H_{ij}}{\sigma_{ij}\sqrt{2\pi}}$), which is proportional to the coefficient H_{ij} and σ_{ij} value of the corresponding CG pair site (ij).

CG model and interactions of Gag and ESCRT-I

To model the ESCRT-I headpiece, UEV, and stalk we used the same CG mapping and interaction parameters as in our previous study of ESCRT-I oligomerization templated by the immature Gag lattice (36). To allow ESCRT-I/II association, the first particle of CG VPS28-CTD was attached to the last particle of the VPS28 N-terminal domain in the headpiece through a harmonic bond of force constant 50 kcal/mol/nm^2 and equilibrium distance 0.15 nm. The updated ESCRT-I CG model contains 109 CG sites. The attractive interactions driving ESCRT-I oligomerization is modeled with pairwise Gaussian potential. The interaction parameters are described in (36). In brief, the value of H_{ij} (−0.9 nm kcal/mol) is chosen such that the ESCRT-I molecules do not oligomerize in the solution. However, the value of H_{ij} is strong enough to allow extensive oligomerization when templated by the immature Gag lattice of appropriate diameter. The CG model of the Gag polyprotein consists of MA, CA/SP1, and nucleocapsid (NC) domains. To model the association of the ESCRT-I UEV domain and p6 domain of Gag, a CG binding site was added to the C-terminal end of the NC domain. Attractive interactions are added between the Gag binding site and the final two C-terminal CG sites of the UEV domain and the Gag binding site. The details of the Gag CG model generation and ESCRT-I/Gag interactions are described in (36).

CG interactions between protein and lipid

All membrane association interactions between the protein CG sites (Gag and ESCRT-II) and the CG lipid headgroup were modeled using a 12-6 Lennard-Jones potential (E_{sclj}) with a modified soft-core (82), $4\varepsilon\lambda^n[1/(\alpha_{LJ}(1-\lambda)^2+(r/\sigma)^6)^2 - 1/(\alpha_{LJ}(1-\lambda)^2+(r/\sigma)^6)]$. Here, $n=2$, $\alpha_{LJ}=0.5$, $\lambda=0.6$, and $\sigma=1.5$ nm. Gag interacts with the lipid headgroup through three beads in the N-terminal region of the MA domain with an interaction strength, $\varepsilon=2.5$ kcal/mol. ESCRT-II interacts with the lipid headgroup with an optimal interaction strength, $\varepsilon=3.0$ kcal/mol. We note that, in the main text, the membrane association strength of ESCRT-II ($E_{\mathrm{Esc\text{-}II/Mem}}$) is identical to ε. For ESCRT-II, we also explored lower interaction strengths varying ε ($E_{\mathrm{Esc\text{-}II/Mem}}$) from 1.5 to 2.5 kcal/mol.

The CG atom type index of the composite system is listed in Table S1. The details of the attractive interactions that drive ESCRT-I/II association and ESCRT-I oligomerization are listed in Tables S2 and S3, respectively. Additional details on the CG model bonding topology, hENM force constant, equilibrium bonding distances, and coordinates of the initial CG models are deposited in https://github.com/arpahudait/Gag-ESCRT_budding.

CG MD system setup and simulation settings

We prepared the "*bud neck*" model system resembling the budding site of the immature HIV-1 virion with the same protocol as in our previous CG

study (36). In brief, we prepared model Gag shells by extracting coordinates of the Gag polyprotein assemblage from cryoelectron microscopy maps of immature HIV-1 lattices. The diameter (D_{Gag}) of the inner aperture of the Gag shell for all systems in this study is 50 nm. This is the optimal dimension for the 12-membered ESCRT-I ring formation (36). The extracted Gag lattice was then mapped to CG Gag and wrapped with a membrane surface that resembles a budding neck. The final lateral dimension of the simulation cell was 136 × 136 nm in the x, y directions, respectively. The system was then equilibrated for 10 × 10^6 CG timesteps by integrating only the CG lipids (the protein is held fixed) to allow relaxation of the lipid sheet and neck. During the same equilibration period, lipids wrapping the Gag establish contact with the MA domain of the Gag. For all the production run simulations, the lipids in contact with the topmost layer of Gag hexamer in the shell (Fig. 4) were identified. These lipid molecules were kept frozen to prevent the collapse of the lipid due to the presence of the open edge in the partial virion setup in our simulations. The 12-membered ESCRT-I ring was then manually docked to the Gag shell. The system was then further equilibrated for 20 × 10^6 CG timesteps. In these simulations, the CA/SP1 domain of the Gag is held fixed, while other domains of the Gag, ESCRT-I, and lipids are allowed to fluctuate. In the immature virion, the CA/SP1 domain forms a hexameric lattice. Hence, constraining the coordinates of the CA/SP1 domain maintains the lattice separation between Gag neighbors at the high-resolution cryoelectron tomogram values. We found that, in 20 × 10^6 CG timesteps, the UEV domain of all 12 ESCRT-I molecules binds to the Gag. To generate the initial configuration for the simulations of ESCRT-I oligomerization, the attractive interactions between the ESCRT-I proteins that drive oligomerization were turned off, and the system evolved for 50 × 10^6 CG timesteps. During this simulation, the ESCRT-I ring completely disassembles, and the ESCRT-I molecules randomly diffuse in the Gag lumen generating randomized initial configurations. To summarize, we generated two systems 1) ESCRT-I is fully assembled to a 12-membered ring and 2) 12 ESCRT-I monomers are bound to the Gag lattice, however, fully disassembled. To prepare simulations with ESCRT-II, 16 ESCRT-II proteins were initially arranged in a two-dimensional (2D) uniform grid and placed in the xy plane 2 nm above the membrane surface. In addition, the initial ESCRT-II grid was prepared such that the distance between the Gag shell center and ESCRT-II proteins was less than 60 nm. Finally, the system was equilibrated for 20 × 10^6 CG timesteps by turning off the ESCRT-I/II interactions to allow the ESCRT-II proteins to bind to the membrane.

CG MD simulations were performed using the LAMMPS MD software interfaced with PLUMED (version 2.7) (83,84). In all CG MD simulations, the equations of motion were integrated with the velocity Verlet algorithm using a timestep (τ_{CG}) of 50 fs. Periodic boundary conditions were used in the x, y directions. In the z direction, the simulation cell was nonperiodic; hence, the particles cannot move from one side of the box to the other side along the z direction. This is necessary since the z axis of the simulation cell is the direction of budding away from the cytoplasm. The simulations were performed in the constant $Np_{xy}T$ ensemble. The pressure in the xy direction was controlled at 0 bar with the Nose-Hoover barostat using a coupling constant of 2000 τ_{CG} (85). The temperature of the simulation was maintained at 300 K using a Langevin thermostat using a coupling constant of 1000 τ_{CG} (86). Simulation trajectory coordinates were saved every 1 × 10^6 CG MD timesteps.

CG metadynamics simulations

We performed well-tempered metadynamics simulations to facilitate oligomerization of ESCRT-I and binding of ESCRT-II to ESCRT-I at the bud neck. We performed two sets of metadynamics simulations: 1) investigating ESCRT-I oligomerization dynamics (with and without ESCRT-II) and 2) ESCRT-II binding to the fully oligomerized 12-membered ESCRT-I ring. To facilitate oligomerization of ESCRT-I we used the collective variable (CV1) reported in (87). To define CV1, we first represent each ESCRT-I monomer by the geometric center of the CG sites corresponding to headpiece region. This choice is justified since ESCRT-I oligomerization is driven by interactions at the headpiece region (36). To assess the overall connectivity between the ESCRT-I oligomers, we first calculated the coordination number and then a symmetric adjacency matrix using the coordination number. Both coordination number and elements of the adjacency matrix were calculated using a cubic harmonics function with a radial cutoff of 3.5 nm, while the function decays from one to zero between 3.5 and 4 nm (88,89). Then, oligomer sizes were determined by applying the depth first search clustering algorithm to the adjacency matrix. Finally, the value of CV1 is the sum of the coordination numbers for all the ESCRT-I molecules in the largest cluster determined by the depth first search clustering protocol. To define CV2, we first represented each ESCRT-I and ESCRT-II by the geometric center of the CG sites corresponding to the VPS28-CTD and VPS36 linkers, respectively. Then, the distances (D_{ij}) between all ESCRT-I/II pairs were calculated. Finally, CV2 is defined as the maximum of all D_{ij} values. For simulations of ESCRT-I oligomerization in the presence of ESCRT-II the biases were deposited along CV1 and CV2. For simulations of ESCRT-II binding to the 12-membered ring the biases were deposited along CV2.

To improve computational efficiency, a weak harmonic restraint of force constant 2390 kcal/mol/nm^2 was applied to prevent CV2 exceeding 60 nm. In the CG metadynamics simulations, the added Gaussian biases had a width of 0.1 (CV1) and 0.02 nm (CV2). The height of the Gaussian biases was set to 0.15 kcal/mol and was deposited every 500 τ_{CG} with a bias factor of 100.

CG US simulations

To assess the binding free energy between ESCRT-II and membrane, we used US simulations. US simulations were performed as a function of the distance between the center of the membrane and ESCRT-II. To calculate the center of mass of ESCRT-II, only the CG sites of the VPS22:VPS36 subcomplex were considered, since the VPS25 subunits do not associate with the membrane. We restrained the distance at each umbrella window with a harmonic force constant of 200 kcal/mol/nm^2. In the US simulations, the dimension of the membrane surface was 50 × 50 nm in the x, y directions. The distance between the membrane center and ESCRT-II was varied from 3.2 to 18.2 nm generating 150 windows at 0.1 nm. For each window, simulations were evolved for 2 × 10^6 CG MD timesteps. The PMF profile was computed from the final 1.5 × 10^6 CG MD timesteps of each US window using the weighted histogram analysis method (73,74). US simulations were performed by varying $E_{Esc\text{-}II/Mem}$ from 1.5 to 3.0 kcal/mol at intervals of 0.5 kcal/mol. For each $E_{Esc\text{-}II/Mem}$ value, three independent US simulations were generated. The error bar for the binding affinity was calculated from the three PMF profiles at the umbrella window corresponding to the minima.

CG analysis

To identify protein-protein association, we used the following distance-based criteria:

$$d_{P1-P2} = \left| \frac{1}{N_{P1}} \sum_{i=1}^{N_{P1}} r_{P1(i)} - \frac{1}{N_{P2(j)}} \sum_{j=1}^{N_{P2}} r_{P2(j)} \right| \quad (1)$$

where $P1(i)$ and $P2(j)$ are the indices of the CG site types used for the calculation in proteins P1 and P2, respectively. $r_{P1(i)}$ and $r_{P2(j)}$ denote coordinates of the CG sites used for the calculation. N_{P1} and N_{P2} are the number of CG sites used for the calculation in protein $P1$ and $P2$. $d_{P1\text{-}P2}$ is the distance between a specific protein pair. To determine ESCRT-I/II association, we considered CG site types 87–90, 94, and 98–99 of ESCRT-I and CG site types 81 and 89–92 of ESCRT-II. A protein pair was classified as associated if $d_{P1\text{-}P2}$ is less than 3.5 nm.

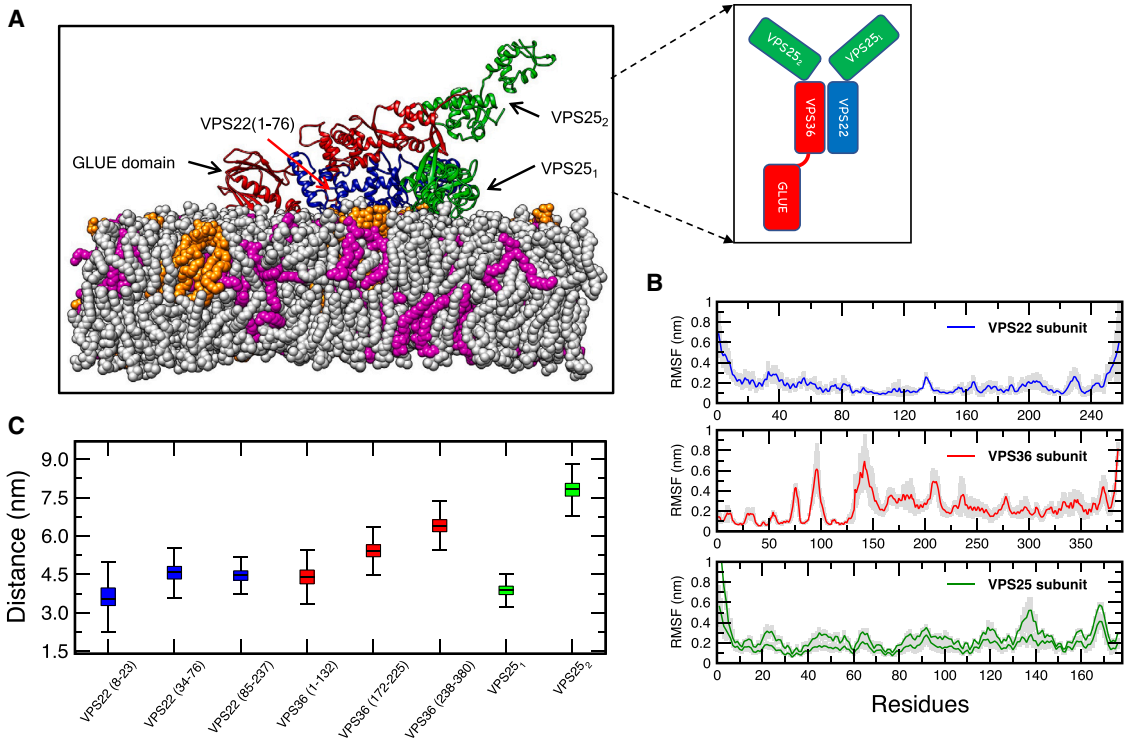

FIGURE 1 All-atom MD simulations of the ESCRT-II complex bound to the membrane. (*A*) Ribbon representation of the full-length ESCRT-II complex bound to POPC (76%):POPE (20%):PIP2 (4%) membrane. The POPC, POPE, and PIP2 lipids are shown in silver, magenta, and orange spheres, respectively. VPS22, VPS36, and VPS25 subunits of ESCRT-II are shown in blue, red, and green ribbons, respectively. VPS25$_1$ and VPS25$_2$ labels are used to denote VPS25 subunits associated with the C-terminal region of VPS22 and VPS36 subunits, respectively. Regions of the protein complex discussed in the text are labeled. Schematic of the four subunits of ESCRT-II, colored blue (VPS22), red (VPS36), and green (VPS25) is shown in the inset. The GLUE domain, which is part of the VPS36 subunit, is also labeled. (*B*) Root mean-square fluctuations (RMSFs) of individual residues for each subunit of the ESCRT-II complex. The solid line represents the mean, and the shaded region represents the standard deviation. The mean and standard deviation for each residue is calculated from the final 1000 ns of each replica trajectory. (*C*) Boxplots of the distance between the center of mass of ESCRT-II regions (residues specified in parentheses) to the membrane center. The boxplots (mean and standard deviation) are prepared from the final 1000 ns of each replica trajectory. To see this figure in color, go online.

RESULTS

Atomistic simulations demonstrate that multiple PIP2-binding sites regulate the membrane-bound orientation of the ESCRT-II complex

ESCRT-II is a Y-shaped heterotetramer complex consisting of one VPS22 and VPS36 subunit and two VPS25 subunits (37,90). The two VPS25 subunits each form an arm of the Y-shaped complex, while the VPS22:VPS36 subcomplex constitutes the stalk of the Y-complex (Fig. 1 *A*). The VPS36 subunit is capped by the membrane-targeting N-terminal (GLUE) domain (VPS36: residues 1–132), while the second membrane-associating VPS22-H0 helix (VPS22: residues 1–23) is in the stalk. AA MD simulations are designed to provide a molecular view of the protein-membrane interactions and the overall membrane-bound conformation of proteins. Here, we performed 2000 ns long AA MD simulations (three replicas) of the full-length ESCRT-II complex binding to a PIP2 containing model membrane. Our objective here was to identify the specific protein residues that make PIP2 contacts and characterize the membrane-bound orientation of the different regions of the heterotetramer ESCRT-II complex.

In the initial configuration, the ESCRT-II complex was positioned near the bilayer, with the lipid-binding basic patch of the GLUE domain and VPS22-H0 helix facing toward the surface of the membrane. The AA MD simulation setup is described in the materials and methods. To identify the PIP2-targeting regions of the protein, we calculated the frequency of PIP2 contacts (averaged over three replicas) for all residues in the VPS22 and VPS36 subunits (Fig. S2). Analysis of root mean-square fluctuations reveals that the loop connecting β6 and β7 (VPS36: 87–105) in the GLUE domain, VPS36 linker (VPS36: 132–171), and C-terminal WH2 domain of VPS25 are particularly plastic (Fig. 1 *B*). We note that these regions do not specifically target PIP2 lipids. In all the simulations, residues in the membrane-targeting basic pockets of the GLUE domain make persistent PIP2 contacts. The VPS22 subunit is anchored to the membrane through PIP2-targeting basic residues in the VPS22-H0 helix. Furthermore, our analysis identified that the basic region (VPS22: residues 53–65) also makes stable contact

with PIP2 lipids providing an additional membrane binding interface for the stalk of the ESCRT-II complex. To characterize the orientation of the membrane-bound ESCRT-II complex, we calculated the distance between the geometric center of different regions of the protein to the membrane center from AA MD trajectories (Fig. 1 *C*). We find that the GLUE domain (VPS36: residues 1–132) and membrane-targeting regions of the VPS22 subunit (residues: 1–76) lie flat on the membrane, associated with the membrane by interactions through multiple PIP2-binding sites. In contrast, the C-terminal region of the VPS36 subunit (residue: 172–380) and the VPS25 subunit associated with the C-terminal region of the VPS36 subunit orients away from the membrane. The other VPS25 subunit associated with the C-terminal region of the VPS22 subunit is aligned parallel to the membrane surface despite not targeting PIP2 lipids.

Taken together, the AA MD simulations indicate that the full-length ESCRT-II complex effectively targets the membrane using a multivalent mechanism, i.e., simultaneously engaging multiple PIP2-binding sites. Our simulations establish an atomistic view of the membrane-bound ESCRT-II complex in which multiple PIP2-targeting residues in the GLUE domain and VPS22 subunit generate an extended and flat membrane-facing surface. Furthermore, we use the membrane-bound atomistic configuration of ESCRT-II complex to systematically derive the CG model and interactions of ESCRT-II with lipids.

CG molecular models of Gag, ESCRT-I, ESCRT-II, and lipid

Our CG MD simulations consist of four components, Gag, ESCRT-I, ESCRT-II, and lipids. In all the CG models used in this study, intradomain interactions are modeled by a heterogeneous harmonic bond network, while interprotein and interdomain interactions are modeled by a combination of excluded volume repulsion to prevent unphysical overlap between the CG beads and short-range attractive interactions to model protein-protein binding (see materials and methods for functional form of the interactions). In our previous study, we developed CG models and interactions of HIV-1 structural protein Gag and upstream ESCRT-I to investigate ESCRT-I oligomerization templated by the immature Gag lattice (36). In brief, CG molecular model of full-length Gag consists of MA, CA/SP1, NC, and p6 domains. The CG molecular model of ESCRT-I consists of headpiece, stalk, UEV domain, and a flexible linker connecting the UEV domain to stalk. The linker provides flexibility to UEV, allowing the UEV to diffuse at the Gag lattice surface. To model ESCRT-I binding to the Gag late domain, attractive interactions were included between the C-terminus of Gag late domain and the final two CG sites at the C-terminal end of the ESCRT-I UEV domain. To model ESCRT-I self-assembly, short-ranged attractive interactions were added to CG sites corresponding to residues in the human ESCRT-I headpiece involved in direct electrostatic contacts in the crystallographic structure of the 12-membered ring. The strength of the attractive interactions was chosen such that ESCRT-I does not oligomerize in the solution, mimicking experimentally observed behavior of ESCRT-I. However, the strength of the attractive interactions was sufficient to drive self-assembly of ESCRT-I when templated by an immature Gag lattice (36).

In this work, we developed a bottom-up CG molecular model of ESCRT-II from membrane-bound conformations generated from AA MD trajectories. First, a CG model of ESCRT-II was mapped from AA MD trajectories. The CG model of the ESCRT-II complex contains 222 CG sites with an average resolution of 4.5 amino acid residues per site. To capture intraprotein flexibility, the bonded topology of the CG model and the harmonic force constant of these bonds were derived from AA MD trajectory. Details of CG model development are provided in the materials and methods. In CG MD simulations, the membrane was modeled with a three-site quasi-monolayer highly CG'ed lipid (78). We note that, given the complexity of our multicomponent system, we use a multiscale framework to represent different components of the system (91). A highly CG'ed lipid is used over a more highly resolved CG lipid model to sufficiently increase the computational efficiency of the simulation while retaining adequate physical accuracy. Similarly, a lower resolution for ESCRT-I is used compared with ESCRT-II, as the timescales of ESCRT-I self-assembly are typically slower compared with ESCRT-I/II supercomplex formation. In other words, the CG resolution of each component was optimally chosen to represent key physical features of the protein or lipid and replicate experimentally observed behaviors while maintaining computational efficiency. Finally, we note that, since much of the model is determined bottom-up from structural and AA data rather than by ad hoc fitting of CG models, the issue of mixed CG resolution is less serious. The CG model of all the components simulated in this work is depicted in Fig. 2. The region of each protein that interacts with other proteins or the lipid is also labeled. In the next section, we describe the details of short-ranged attractive interactions between ESCRT-II and other components of the system.

CG attractive interactions of ESCRT-II with lipid and ESCRT-I are derived from atomistic simulations

To model the membrane association of ESCRT-II we first identified CG sites of ESCRT-II that correspond to residues that make persistent PIP2 contacts in AA MD simulations of ESCRT-II bound to membrane. Attractive interactions ($E_{\text{Esc-II/Mem}}$) were added between these CG sites of ESCRT-II and headgroup of CG lipid to model protein-membrane association. To obtain estimates for the membrane association

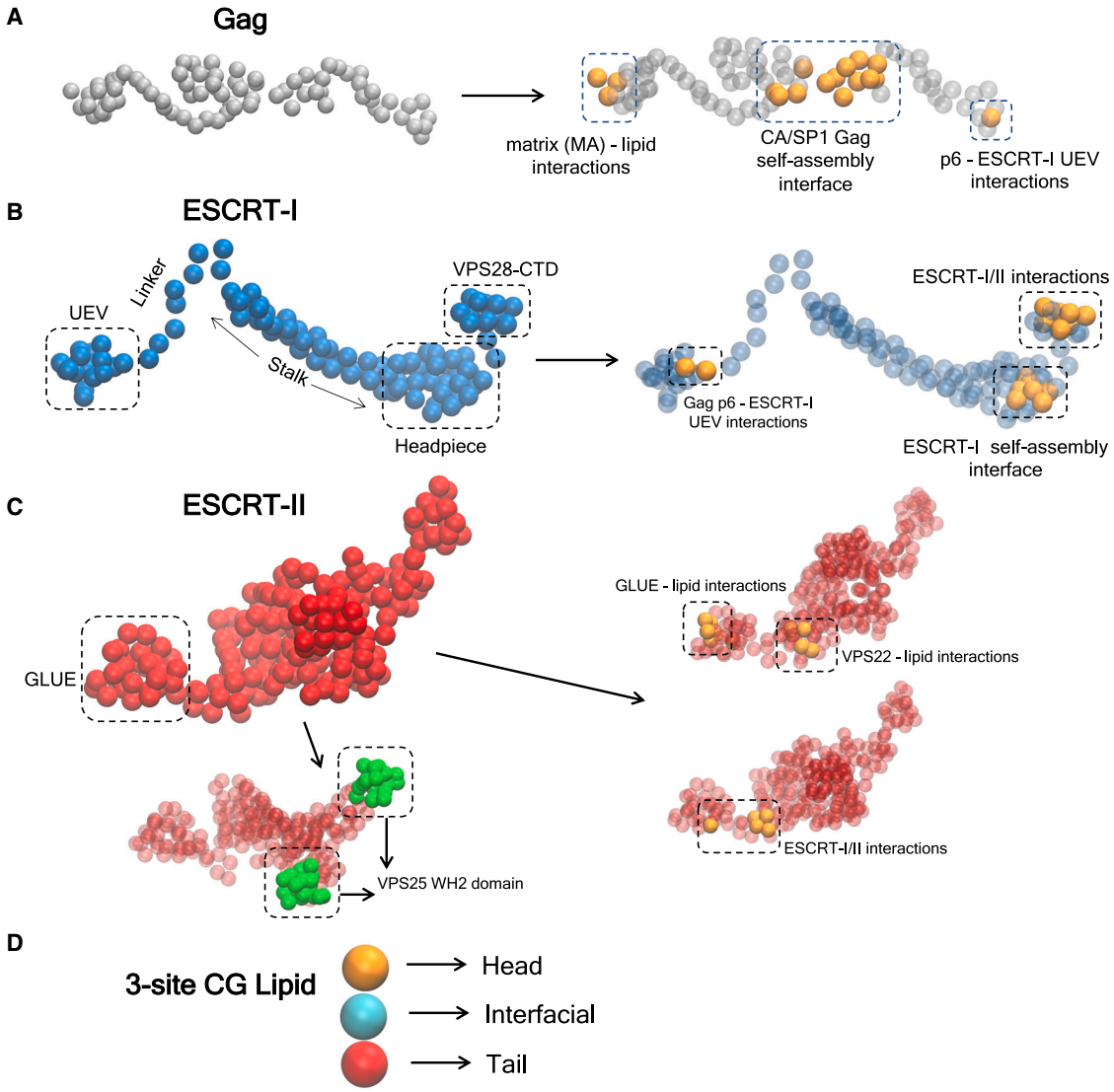

FIGURE 2 Schematic overview and interaction sites of our CG molecular models. (*A*) CG representation of the Gag polyprotein. The orange beads in the right panel denote CG sites with attractive interactions with other proteins and lipids. Gag interacts with CG lipid headgroup through sites in the N-terminal region of MA domain. ESCRT-I UEV domain is allowed to bind to the C-terminal site of p6 domain. We note that, in this study, the CA/SP1 domain of the Gag is constrained to maintain the Gag monomers at the initial crystallographic position. This is required since we use a partial virion construct instead of a full immature virion. Hence, attractive interactions between CG sites at the CA/SP1 self-assembly interface are not relevant to this study. All CG sites with relevant short-ranged attractive interactions with other components are shown in orange spheres. (*B*) CG representation of the ESCRT-I protein. UEV domain, linker connecting UEV and stalk, "rod-like" stalk, headpiece region, and ESCRT-II binding VPS28-CTD domain are labeled. The binding interface with Gag p6, ESCRT-I self-assembly interface in the headpiece, and ESCRT-I/II interacting sites in VPS28-CTD are labeled as orange spheres. (*C*) CG representation of the ESCRT-II protein (*upper left panel*). In the lower left panel, the ESCRT-III binding regions of ESCRT-II (VPS25 WH2 domain) are shown in green spheres. In the right panel, membrane binding CG sites of GLUE domain and VPS22 subunit and CG sites involved in ESCRT-I association through short-ranged attractive interactions are shown in orange spheres. (*D*) Three-site CG lipid is shown with the head, interfacial, and tail beads labeled. To see this figure in color, go online.

interaction strength of CG ESCRT-II we first quantified the binding affinity of the membrane-targeting domains of the AA ESCRT-II complex. To calculate the binding affinity, we constructed PMF profiles of protein binding and unbinding from AA US simulations (details of the US simulation procedure are provided in the materials and methods). For US simulation, we used the distance between the center of lipid bilayer and protein as the reaction coordinate. We note that calculating the PMF profiles of full-length ESCRT-II complex in AA MD simulations is prohibitively expensive due to overall system size. Hence, for AA US simulations we considered GLUE domain and membrane-targeting region of a VPS22 subunit ($VPS22_{Mem}$). Here, $VPS22_{Mem}$ (VPS22: residues 1–76) encompasses both membrane binding regions of VPS22 as observed in AA MD simulations of ESCRT-II complex.

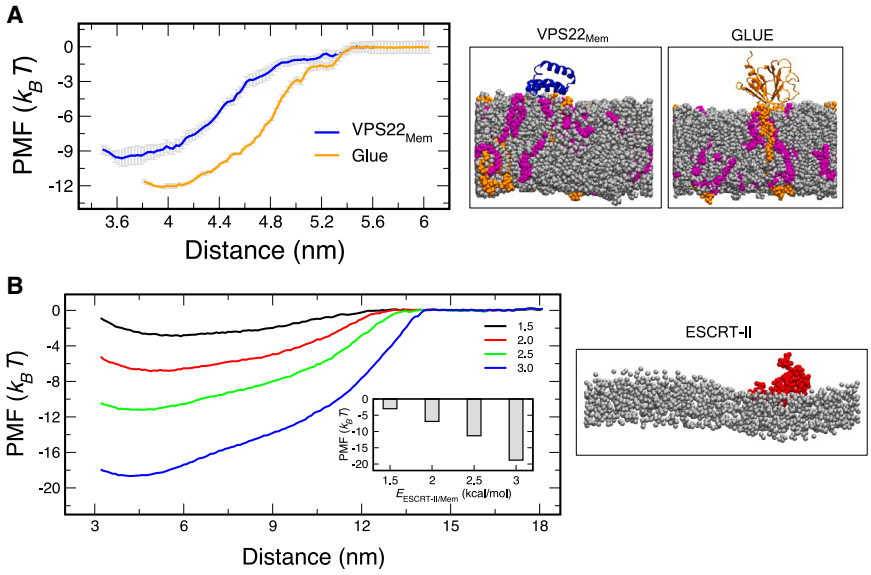

FIGURE 3 Characterization of ESCRT-II and lipid binding interactions. (*A*) Potential of mean force (PMF) for atomistic GLUE monomer and VPS22$_{Mem}$ binding to the membrane. Error bars (shown in *silver* in the background) indicate standard deviation of the PMF calculated from block analysis. The snapshots show membrane-bound state at the free energy minima. The POPC, POPE, and PIP2 lipids are shown in silver, magenta, and orange spheres, respectively. (*B*) PMF for full-length CG ESCRT-II complex binding to the membrane. From top to bottom, each line represents a different $E_{Esc\text{-}II/Mem}$ (attractive interaction between headgroup of CG lipid and membrane-targeting CG site of ESCRT-II). $E_{Esc\text{-}II/Mem}$ is varied from 1.5 to 3.0 kcal/mol. Inset panel shows binding affinity (value at the minimum of the curve) for each $E_{Esc\text{-}II/Mem}$. The snapshot shows membrane-bound state at the free energy minima of the full-length CG ESCRT-II complex. To see this figure in color, go online.

The calculated AA binding affinity is -12 k_BT for the GLUE domain and -10 k_BT for VPS22$_{Mem}$ (Fig. 3 *A*). Our results demonstrate that both membrane-targeting regions of ESCRT-II complex exhibit comparable membrane binding affinity, and agree with liposome binding assay experiments of ESCRT-II deletion constructs (37). We approximate that the binding affinity of the full-length ESCRT-II complex is a combination of the contributions from GLUE and VPS22$_{Mem}$ regions (-22 k_BT). Using AA binding affinity estimate we evaluated the appropriate $E_{Esc\text{-}II/Mem}$ for the full-length CG ESCRT-II model. To do so, we varied $E_{Esc\text{-}II/Mem}$ and calculated the binding affinity of CG full-length ESCRT-II to the membrane for each $E_{Esc\text{-}II/Mem}$ from US simulations (details of CG US simulations is provided in the materials and methods). We find that, at $E_{Esc\text{-}II/Mem} = 3.0$ kcal/mol, the binding affinity (-20 k_BT) of the CG ESCRT-II complex (Fig. 3 *B*) closely reproduces the binding affinity of the AA ESCRT-II complex (-22 k_BT). Therefore, our choice of $E_{Esc\text{-}II/Mem}$ designed to mimic the binding affinity of AA complex supports the validity of CG protein-lipid interactions used in this study.

Previous biochemical data have indicated that ESCRT-I VPS28-CTD binds to VPS36 linker (VPS36: residues 140–169) of ESCRT-II (37,38). This interaction drives ESCRT-I/II supercomplex formation. To derive ESCRT-I/II CG interactions, we first generated a heterodimer complex of ESCRT-II VPS36 linker (residues: 140–169) and ESCRT-I VPS28-CTD (residues: 107–203) in AlphaFold2-Multimer (92). The heterodimer model was then aligned with the membrane-bound ESCRT-II VPS22:VPS36 subcomplex generated from AA MD simulations of the full-length ESCRT-II complex described in the previous section. The membrane-bound protein multimeric complex of ESCRT-I VPS28-CTD, and ESCRT-II VPS22:VPS36 subunits was then evolved for 1 μs at atomistic resolution to examine the contacts established by the ESCRT-I VPS28-CTD with ESCRT-II. In the simulation trajectory, the VPS28-CTD domain forms excess contacts (Fig. S3) with residues in the C-terminal region of the GLUE domain (VPS36: residues 1–132) in agreement with pull-down experiments of ESCRT-II deletion constructs (37). Therefore, using the generated AA MD trajectories to derive the ESCRT-I/II CG interactions supports the validity of these CG interactions used to model ESCRT-I/II supercomplex formation. We then systematically derived ESCRT-I/II CG interactions ($E_{Esc\text{-}I/II}$) from the generated reference AA trajectories using relative entropy minimization (see materials and methods for details) (79). Here, we note that the initial atomic configuration of the ESCRT-I/II supercomplex, specifically at the ESCRT-I VPS28-CTD and N-terminal end of the VPS36 subunit of ESCRT-II, is generated from AlphaFold2-Multimer. Since unbiased AA MD simulations are time limited, alternative interactions between the ESCRT-I VPS28-CTD and other subunits of ESCRT-II cannot be ascertained from our simulations. Therefore, in the future additional enhanced sampling simulations of ESCRT-I/II supercomplex need to be performed to determine these alternative binding interactions and the relative strengths of these interactions.

In our simulations of ESCRT-I oligomerization (described in the following sections) we do not include any attractive binding interactions between ESCRT-II and ESCRT-II. We note that a previous study had reported ESCRT-II clustering only in the presence of cholesterol in lipid nanodomains, thus indicating weak direct interactions between ESCRT-II monomers (93). Our simplified CG lipid model expectedly cannot replicate complex lipid behavior at the viral budding site and therefore induce ESCRT-II

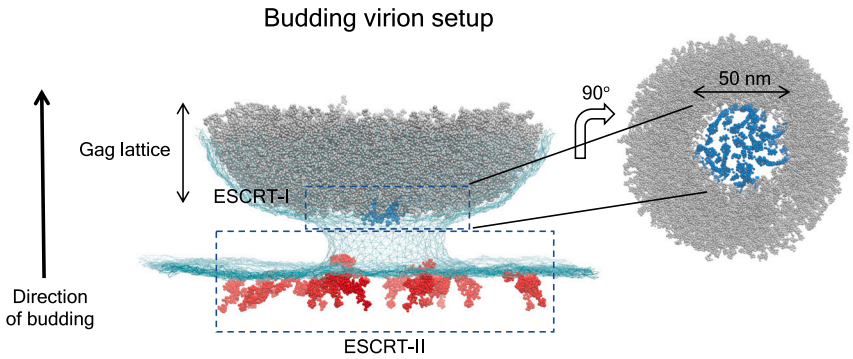

FIGURE 4 Budding virion system setup in CG MD simulations. Composite system setup of immature Gag virion and upstream ESCRT components is shown in the left panel. Gag lattice shell is shown in gray, ESCRT-I in blue, and ESCRT-II in red spheres. Initially, 16 copies of ESCRT-II are randomly distributed at the flat section of the membrane. The membrane is shown in cyan mesh. The upward arrow indicates the direction of the viral budding, i.e., budding away from the cytoplasm. A rotated and close-up view of the Gag aperture with 12 copies of ESCRT-I bound to Gag and fully disassembled is also shown in the right panel. To see this figure in color, go online.

clustering. Finally, there is no attractive binding interaction between Gag and ESCRT-II, since any direct interaction between these proteins is yet to be characterized structurally or biochemically.

ESCRT-I effectively oligomerizes in the presence of ESCRT-II at bud neck

Our previous CG MD simulations demonstrated that higher-order ESCRT-I complexes preferentially oligomerize when the diameter of the inner aperture of the Gag lattice is 54–63 nm (36). Different from our previous study, in this work, our intention is to determine the assembly competence of ESCRT-I templated by the Gag lattice in the presence of ESCRT-II. The system in our CG MD simulations is created such that it mimics a budding immature virion in the late stages of immature lattice growth when the underlying membrane is significantly deformed (60,94). Hence, our system consists of a hemispherical Gag shell wrapped with the membrane emulating a narrowing bud neck (Fig. 4). The hemispherical Gag shell used in this work is a partial virion construct and is created by slicing a section from a cryoelectron tomography structure of a near-spherical immature Gag virion (see materials and methods for details). We note that ESCRTs colocalize at the edge of the immature virion. Hence, simulating the entire immature virion is redundant for the purpose of this study. The aperture diameter of the Gag lattice in our simulation is ~50 nm. The initial membrane bud neck dimension closely follows the initial aperture diameter of the Gag lattice. The diameter of the inner aperture of the Gag lattice is comparable with the outer diameter (~50 nm) of the 12-membered ESCRT-I ring formed by outward projecting UEV domains. We prepared our simulations with 12 copies of ESCRT-I monomers bound to the Gag lattice in a fully disassembled state. In addition, 16 copies of ESCRT-II were placed randomly at the flat section of the membrane surrounding the bud neck opening in the simulations with ESCRT-II. Since ESCRT-I and -II form 1:1 supercomplexes, we deliberately used a stoichiometric excess of ESCRT-II. The simulations reported in this section mimic events during which both ESCRT-I and -II colocalize at the viral budding site at the late stages of immature Gag lattice assembly.

We simulated ESCRT-I oligomerization using well-tempered metadynamics (WTMetaD) to estimate the optimal ESCRT-I oligomer size and investigate differences between assembly behavior with and without ESCRT-II (95,96). We note that WTMetaD simulations were used to accelerate ESCRT-I assembly to improve the timescales of ESCRT-I assembly dynamics observed in our previous unbiased simulations (36). We prepared triplicate simulations for both cases (with and without ESCRT-II), and the simulations evolved for 200×10^6 CG MD timesteps (τ_{CG}). In WTMetaD CG MD simulations, we biased the sum of the coordination number of the largest ESCRT-I oligomer in the system as a collective variable (CV) to enhance ESCRT-I assembly (87). Then we reweighted the trajectories to calculate the probability distribution of largest ESCRT-I oligomer size observed in our simulations (97,98). For CG MD simulations with ESCRT-II, a second CV was used to characterize the likelihood of ESCRT-II diffusing to the bud neck. Additional details on the CVs and WTMetaD CG MD simulations are provided in the materials and methods. We note that, in all simulations, the binding strength of ESCRT-II lipid binding sites and CG lipid headgroup is 3.0 kcal/mol unless mentioned otherwise. ESCRT-I/II binding was modeled using CG interactions ($E_{\text{Esc-I/II}}$) derived from AA simulations described in the previous section.

To characterize the dynamics of ESCRT-I oligomerization, we calculated the largest ESCRT-I oligomer size in our WTMetaD simulation trajectories. The time profiles of the largest ESCRT-I oligomer size in simulations with and without ESCRT-II are shown in Fig. 5 *A*. As seen in Fig. 5 *A*, ESCRT-I readily self-assembles in the absence of ESCRT-II to higher-order oligomers, initially up to a 7-mer. The largest ESCRT-I oligomer then spontaneously grows by attachment of adjacent monomers or small oligomers. Interestingly, multiple times during the simulations, we observed the coalescence of the largest oligomer and intermediate clusters to a 12-membered ring. The 12-membered ring typically had a short lifetime and

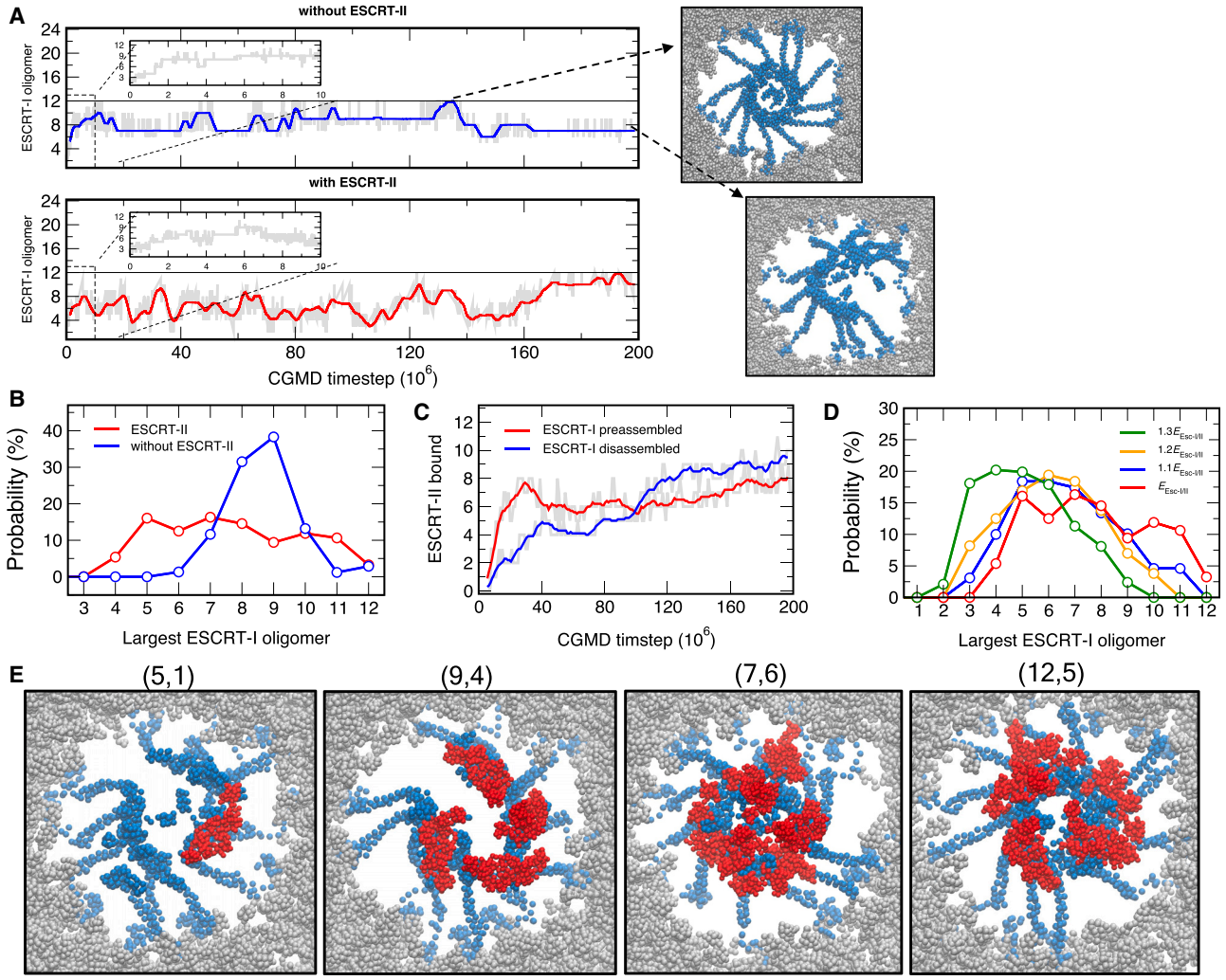

FIGURE 5 Dynamics of ESCRT-I oligomerization and ESCRT-I/II supercomplex formation. (*A*) Time series profile of ESCRT-I oligomerization (largest oligomer size) without ESCRT-II (*top panel*) and with ESCRT-II (*bottom panel*) from the WTMetaD CG MD simulations. The faded region in gray is the raw data depicting the largest ESCRT-I oligomer. The solid line is the blocked moving average calculated over 1×10^6 timesteps for 200×10^6 timestep long trajectories. The horizontal solid line (*black*) denotes oligomerization to the 12-membered ring. The top snapshot indicates oligomerization of ESCRT-I to the 12-membered ring during the simulation trajectory. The bottom snapshot indicates the 9-mer from the endpoint of simulation trajectory. We note that only the largest oligomer is shown for clarity. (*B*) Probability distribution of the largest ESCRT-I oligomer size in the simulation without ESCRT-II (*blue*) and with ESCRT-II (*red*) was presented after reweighting the WTMetaD trajectories. The probability distribution is calculated from final 100×10^6 timesteps of three replicas for each system. (*C*) Time series profile of ESCRT-II recruitment in simulations with ESCRT-I fully disassembled in the initial configuration (*solid blue line*), and ESCRT-I preassembled to the 12-mer ring in the initial configuration (*solid red line*). The solid lines are the running average calculated over 5×10^6 timesteps. The shaded background is the raw data. (*D*) Probability distribution of the largest ESCRT-I oligomer size in the simulation with ESCRT-II when ESCRT-I/II interaction strength is varied. The probability distribution of CG ESCRT-I/II interaction strength ($E_{\text{Esc-I/II}}$) derived from all-atom simulations is shown in red, 10% stronger ($1.1\ E_{\text{Esc-I/II}}$) shown in blue, 20% stronger ($1.2\ E_{\text{Esc-I/II}}$) shown in orange, and 30% stronger ($1.3\ E_{\text{Esc-I/II}}$) shown in green. (*E*) Snapshots (top view looking into the aperture of the Gag lattice from the bud neck) from the simulations of ESCRT-I oligomerization and ESCRT-II recruitment. Gag, ESCRT-I and ESCRT-II are shown in silver, blue, and red spheres, respectively. Each snapshot is titled as (N_1, N_2), where N_1 is the largest ESCRT-I oligomer in the system, and N_2 is the number of ESCRT-II copies bound to ESCRT-I. The CG lipid beads are not shown for clarity. To see this figure in color, go online.

underwent partial disassembly due to the detachment of monomers or small oligomers from the edge of the ring. We then calculated the cumulative probability distribution of the largest ESCRT-I oligomer size (Fig. 5 *B*) from the final 100×10^6 CG MD timesteps of all replicate simulations. The largest ESCRT-I oligomer typically fluctuates between a 7-mer and 9-mer, constituting ~80% of the largest ESCRT-I oligomer distribution observed in these simulations. The results here establish the assembly competence of ESCRT-I when templated by the late-stage immature Gag lattice of optimal geometry (~50 nm aperture diameter).

While an optimal geometry of immature Gag lattice orchestrates ESCRT-I oligomerization, how the presence of

other upstream components at the bud neck influences the oligomerization dynamics of ESCRT-I remains an open question. Therefore, we included multiple copies of ESCRT-II in the vicinity of the bud neck opening and repeated the same simulation of ESCRT-I oligomerization above. The key difference here is that ESCRT-II can diffuse to the bud neck and spontaneously form ESCRT-I/II supercomplexes at the interface of the immature Gag lattice and bud neck. During the simulations, ESCRT-I/II supercomplexes formed in a slow and monotonically increasing manner. The time profile of ESCRT-I/II supercomplexes formed (Fig. 5 *C*) show that the bud neck can accommodate up to seven to nine copies of ESCRT-II. We now discuss ESCRT-I oligomerization behavior again in the presence of ESCRT-II. The time profile of the largest ESCRT-I oligomer size shows that ESCRT-I monomers rapidly self-assembled to higher-order oligomers, exhibiting comparable assembly dynamics as in the simulations without ESCRT-II. It is noteworthy that, in the presence of ESCRT-II, we observe increased fluctuation in the largest ESCRT-I oligomer size, which indicates that ESCRT-I oligomers are now more likely to partially disassemble and then regrow. Cumulative probability distribution of the largest ESCRT-I oligomer size in the presence of ESCRT-II shows the prevalence of smaller ESCRT-I oligomers (4-mer to 6-mer), in contrast to the assembly behavior of ESCRT-I oligomerization in trajectories without ESCRT-II. Nevertheless, larger ESCRT-I oligomers (7-mer and higher) are also frequently observed in these simulation trajectories. Snapshots of ESCRT-I oligomers bound to ESCRT-II are shown in Fig. 5 *E*. Our simulations demonstrate that ESCRT-I remains assembly competent in the presence of ESCRT-II. However, crowding at the edge of the bud neck due to the localization of multiple ESCRT-II copies and the formation of ESCRT-I/II supercomplexes at the Gag lumen may moderately interfere with ESCRT-I oligomerization dynamics.

We have demonstrated that ESCRT-I is assembly competent in the presence of ESCRT-II, albeit less efficiently than in simulations in the absence of ESCRT-II. The ESCRT-I self-assembly interface in the headpiece region and ESCRT-I/II binding interface (VPS28-CTD) are contiguous to each other (Fig. 2, *B* and *C*). Therefore, the binding of ESCRT-II to VPS28-CTD and the formation of the ESCRT-I/II supercomplex can sterically inhibit the association of ESCRT-I headpieces, hindering self-assembly. Nonetheless, the assembly competence of ESCRT-I in the presence of ESCRT-II observed in our simulations may be a consequence of weak interactions that drive ESCRT-I/II association. In other words, weak ESCRT-I/II interactions likely allow continuous binding and unbinding of ESCRT-I/II supercomplexes. Repeated dissociation events of ESCRT-I/II supercomplexes can alleviate crowding at the Gag lumen and promote self-assembly of the ESCRT-I headpiece. We, therefore, sought to examine this scenario and establish whether the interaction strength of ESCRT-I/II association (comparable with computational mutation) implicitly regulates ESCRT-I oligomerization dynamics. We thus monotonically increased the ESCRT-I/II interaction strength of the AA-derived CG interaction ($E_{\text{Esc-I/II}}$) by 30% and repeated the simulations of ESCRT-I oligomerization in the presence of ESCRT-II at different augmented interaction strengths. The cumulative probability distribution of the largest ESCRT-I oligomer size for these simulations is shown in Fig. 5 *D*. We found that the propensity to observe smaller ESCRT-I oligomers is significantly higher in the simulations with enhanced ESCRT-I/II interaction strength. Therefore, unlike our previous simulations with weak ESCRT-I/II interaction derived from AA reference configurations ($E_{\text{Esc-I/II}}$), an increased interaction strength of ESCRT-I/II association in simulations imparts enhanced kinetic stability to the ESCRT-I/II supercomplexes, impeding extended ESCRT-I assembly.

ESCRT-III binding regions of ESCRT-II are distributed in the proximity of the outer bud neck periphery

In this section, we assess the structural features of ESCRT-I/II supercomplexes formed at the bud neck. Specifically, we are interested in determining the spatial distribution of the C-terminal tip of VPS25 subunits in the bud neck. VPS25 directly recruits ESCRT-III components (39). Therefore, examining the VPS25 position will allow us to provide mechanistic insight from where in bud neck ESCRT-III polymers can nucleate and propagate. To determine the ESCRT-I/II supercomplex structure, we performed CG MD simulations of ESCRT-II association to the fully assembled 12-membered ESCRT-I ring bound to an immature Gag lattice. We prepared triplicate simulations (200×10^6 CG MD timesteps) containing 16 copies of ESCRT-II with an identical simulation setup as described in the previous section. Structural analysis of the ESCRT-I/II supercomplexes was performed from the final 50×10^6 CG MD timesteps over all the replicates.

Visual inspection of ESCRT-I/II supercomplexes formed in the CG MD simulations reveals column-like complexes that scaffold the bud neck (Fig. 6 *A*). To characterize the orientation of the ESCRT-I/II supercomplexes, we calculated the distribution of a distance-based parameter ($D_{\text{E1-VPS25}}$). Here, $D_{\text{E1-VPS25}}$ is defined as the distance between the centroid of a 12-membered ESCRT-I headpiece ring and a C-terminal WH2 domain of ESCRT-II VPS25 subunits along the bud neck axis. Alternatively, for a particular ESCRT-I/II supercomplex, $D_{\text{E1-VPS25}}$ signifies the spatial distribution of VPS25 subunits at the bud neck. The higher the value of $D_{\text{E1-VPS25}}$, the closer the VPS25 tips are to the outer edge of the bud neck or farther away from the immature Gag lattice. We note that the approximate distance of the outer edge of the bud neck and ESCRT-I headpiece

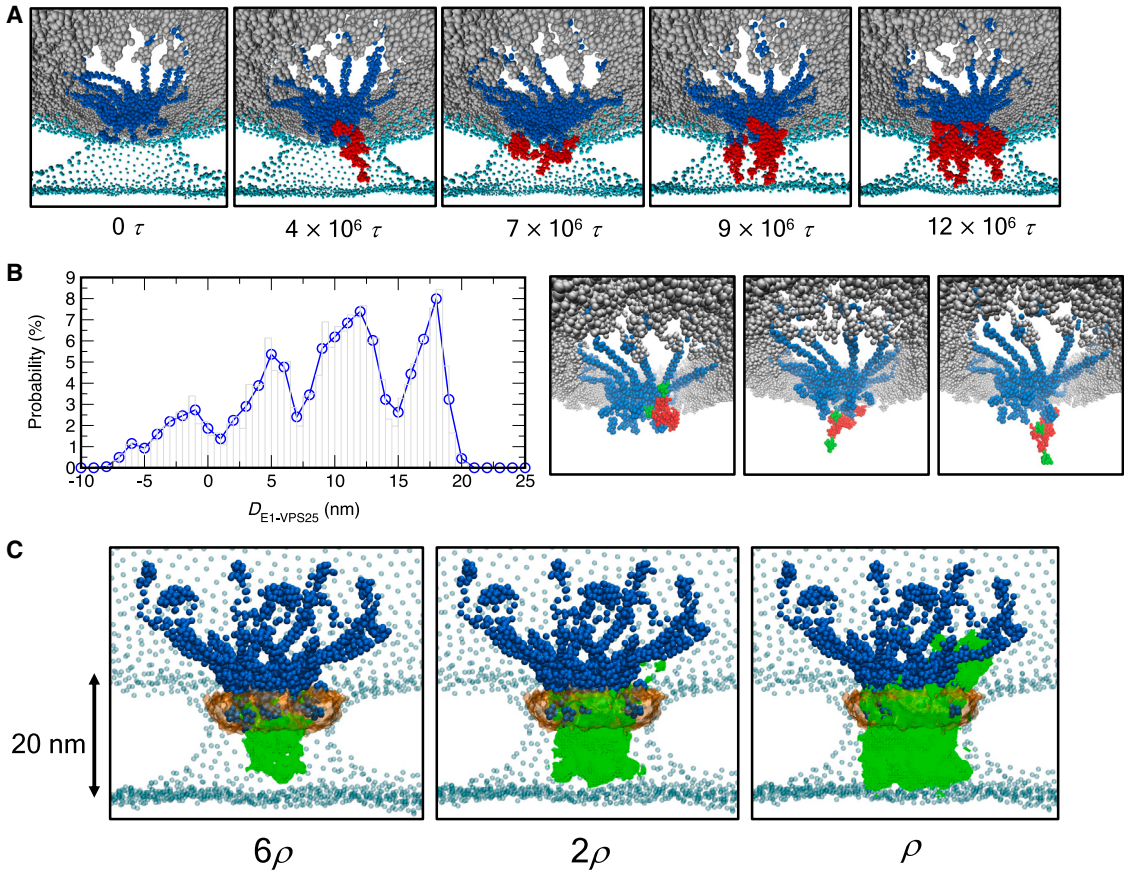

FIGURE 6 Structure of the ESCRT-I/II supercomplex. (*A*) Representative snapshots showing ESCRT-II localization at the bud neck (*side view*) and time series of stepwise recruitment of ESCRT-II by 12-membered ESCRT-I ring at the bud neck. The leftmost panel depicts the bud neck before ESCRT-II recruitment. The next four panels depict sequential ESCRT-II binding events (up to four ESCRT-II copies are shown). The central CG bead of the three-site CG lipid is shown in cyan spheres. Note that the membrane is sliced vertically in snapshots to show the interior of the bud neck and Gag lumen. Gag, ESCRT-I, and ESCRT-II are shown in silver, blue, and red spheres, respectively. (*B*) Probability distribution of $D_{\text{E1-VPS25 was}}$ calculated over the final 50×10^6 timesteps of each replica simulation. Snapshots show different orientations of ESCRT-II, in which both copies of the VPS25 subunit WH2 domain (shown in *green spheres*) are pointing toward the Gag lumen (*left panel*), aligned to the midplane of bud neck (*center*), and one of the VPS25 subunit WH2 domain is pointing toward the outer edge of bud neck (*right*). (*C*) Time-averaged densities of the VPS25 WH2 domain CG sites are shown in green. The densities are contoured at 6ρ, 2ρ, and ρ ($\rho = 1 \times 10^{-5}$) in three snapshots from left to right. We note that the higher the value of density contour, the more likely the probability that VPS25 CG sites are distributed in that region during the simulations. Time-averaged density of CG sites of ESCRT-II involved in lipid binding and ESCRT-I association (contoured at ρ) is shown in orange. All the densities are overlaid onto ESCRT-I 12-membered ring and lipid. Gag is not shown for clarity. CG lipid is shown in cyan spheres. Dimension of the bud neck measured from the plane of 12-membered ESCRT-I headpiece and flat section of membrane is ~20 nm. To see this figure in color, go online.

complex is ~20 nm in our budding virion simulation setup. We find that, for the ~50% population of ESCRT-I/II supercomplex structures observed in our simulations, the $D_{\text{E1-VPS25}}$ value is higher than 10 nm, i.e., VPS25 tips are located above the midplane of bud neck (Fig. 6 *B*). In these ESCRT-I/II supercomplex structures, ESCRT-II predominantly spans from the ESCRT-I headpiece complex (at the inner edge of bud neck proximal to Gag) to the outer edge of the bud neck (distal to Gag) in a vertical column-like orientation. Conversely, for a minor subpopulation of ESCRT-I/II supercomplexes (~12%), $D_{\text{E1-VPS25}}$ values are negative, i.e., VPS25 tips are located below the plane of the ESCRT-I headpiece complex. In these ESCRT-I/II supercomplex structures, C-terminal tips of VPS25 of ESCRT-II are oriented toward the Gag lumen. Next, we investigate the impact of enhancing the ESCRT-I/II interactions, which would increase the stability and lifetime of these ESCRT-I/II supercomplexes. We find that, for enhanced ESCRT-I/II interactions, a nominally higher population of ESCRT-I/II structures (Fig. S4) have the VPS25 tips located below the plane of the ESCRT-I headpiece complex (i.e., negative $D_{\text{E1-VPS25}}$ values). This observation can also rationalize the results presented in the previous section pertaining to how ESCRT-I/II interaction strength modulates ESCRT-I oligomerization. A higher population of misoriented ESCRT-I/II supercomplex structures (negative $D_{\text{E1-VPS25}}$ values) increases molecular crowding at the Gag lumen as the VPS25 tips of ESCRT-II occupy the Gag lumen with greater propensity. Hence, nonspecific crowding of the Gag lumen impedes extended ESCRT-I assembly.

The locus of ESCRT-I binding to ESCRT-II and the membrane-targeting sites of ESCRT-II are in close vicinity (Fig. 2, *B* and *C*). To provide a molecular view of the spatial distribution of proteins at the bud neck, we calculated the time-averaged 3D density of key regions of ESCRT-II proteins bound to the 12-membered ESCRT-I headpiece ring from our simulation trajectories (Fig. 6 *C*). Specifically, we calculated the 3D density distribution of CG sites of ESCRT-II involved in membrane binding and ESCRT-I association, and the CG sites corresponding to the C-terminal WH2 domain of ESCRT-II VPS25 subunits. The latter region recruits ESCRT-III proteins at the bud neck. The density maps reveal that the CG sites of ESCRT-II involved in lipid targeting and ESCRT-I association are spatially distributed above the plane of the 12-membered ESCRT-I headpiece ring. Hence, the inner edge of the bud neck proximal to the Gag lattice is pinned to ESCRT-I/II supercomplexes. Furthermore, the inner edge of the bud neck appears to be highly crowded in the density maps. The density map (contoured at 6ρ) of VPS25 reveals that ESCRT-III binding regions of ESCRT-III are likely to be distributed between the midplane and outer edge of the bud plane, in agreement with the probability distribution of $D_{\text{E1-VPS25}}$ (Fig. 6 *B*). In these ESCRT-I/II supercomplex structures, ESCRT-II VPS25 tips are pointing toward the outer edge of bud neck. We also observed additional subpopulations of ESCRT-I/II supercomplex structures (densities contoured at 2ρ and ρ) in which VPS25 tips are either coplanar to the density corresponding to CG sites of ESCRT-II involved in membrane binding and ESCRT-I association or pointing toward the highly crowded Gag lumen. VPS25 subunits do not have any associative interactions with ESCRT-I or Gag; hence, they are likely to be sterically occluded from the highly crowded inner edge of the bud neck in our simulations. Therefore, the ESCRT-I/II supercomplexes observed in our simulations predominantly form column-like structures, and VPS25 subunits are preferentially distributed closer to the outer edge of the bud neck.

ESCRT-I/II supercomplex formation initiates bud neck constriction

Protein-membrane interactions drive spontaneous change in membrane neck shape. It is well known that proteins can induce membrane neck shape through scaffolding of the membrane by protein complexes (99,100), membrane association and insertion of hydrophobic helices (101,102), and protein crowding on membrane surfaces (57,103). Our simulations show that ESCRT-I/II supercomplexes form column-like assemblies scaffolding the bud neck. Furthermore, we find that multiple copies of ESCRT-II associating with the headpiece of the 12-membered ESCRT-I ring pin the inner edge of the bud neck to the Gag-ESCRT-I complex. We next analyzed how the dynamics of ESCRT-I/II supercomplex formation modulate the dimension of the bud neck from our simulation trajectories. To do so, we first estimated the width of the inner edge of the bud neck (D_{Neck}). We defined the inner edge of the bud neck as the region directly in contact with the CG sites of ESCRT-II involved in lipid targeting and ESCRT-I association (Fig. 7 *A*). Specifically, the inner edge of the bud neck spans from above the plane of the ESCRT-I headpiece ring to approximately the midplane of the bud neck. In the simulation trajectories, we observed the formation of six ESCRT-I/II supercomplexes rapidly within $\sim 20 \times 10^6$ CG MD timesteps, followed by a gradual increase up to the formation of seven to nine ESCRT-I/II supercomplexes. The time profile of the D_{Neck} along the simulation trajectory is shown in Fig. 7 *B*, and the associated snapshots of the bud neck are shown in Fig. 7 *C*. Analysis of the time profile of D_{Neck} indicates that the inner edge of the bud neck monotonically undergoes constriction from 45 to 33 nm through multiple fluctuation events throughout the simulation trajectory (Video S1). Furthermore, bud neck constriction is initiated when multiple ESCRT-I/II supercomplexes are formed. Visualization of the trajectories and the time profiles indicate that multiple copies of ESCRT-II initially localize at the bud neck forming ESCRT-I/II supercomplexes pinning the bud neck to the Gag-ESCRT-I scaffold. Then, the membrane-associating interactions of multiple copies of ESCRT-I-bound ESCRT-II initiate membrane neck constriction by pulling the inner edge of the bud neck toward the ESCRT-I headpiece ring.

To assess whether strong protein-membrane interactions are important for the pinning of the membrane neck to the Gag-ESCRT-I complex and, therefore, stabilizing a highly constricted bud neck, we modified $E_{\text{Esc-II/Mem}}$ from 3.0 to 1.5 kcal/mol. The initial configuration of these simulations with reduced $E_{\text{Esc-II/Mem}}$ is taken from the final configuration of the simulations with $E_{\text{Esc-II/Mem}} = 3.0$ kcal/mol. Simulations with altered $E_{\text{Esc-II/Mem}}$ were then evolved for additional 100×10^6 CG MD timesteps, and the final 50×10^6 CG MD timesteps were used to calculate the width of the inner edge of the bud neck (D_{Neck}). We find that, as the protein-membrane interactions are weakened, the degree of constriction of the bud neck gradually diminishes (Fig. 7 *C*). In other words, for weaker protein-membrane interactions, multiple copies of ESCRT-II can localize at the bud neck and bind to ESCRT-I without inducing significant bud neck constriction. Altogether, our simulations demonstrate that pinning of the inner edge of the bud neck to the Gag-ESCRT-I scaffold is regulated by a network of interactions between immature Gag lattice, ESCRT-I, ESCRT-II, and lipid. The formation of ESCRT-I/II supercomplexes at the budding virion neck initiates neck constriction pulling the inner edge of the bud neck toward the ESCRT-I headpiece ring. Furthermore, these

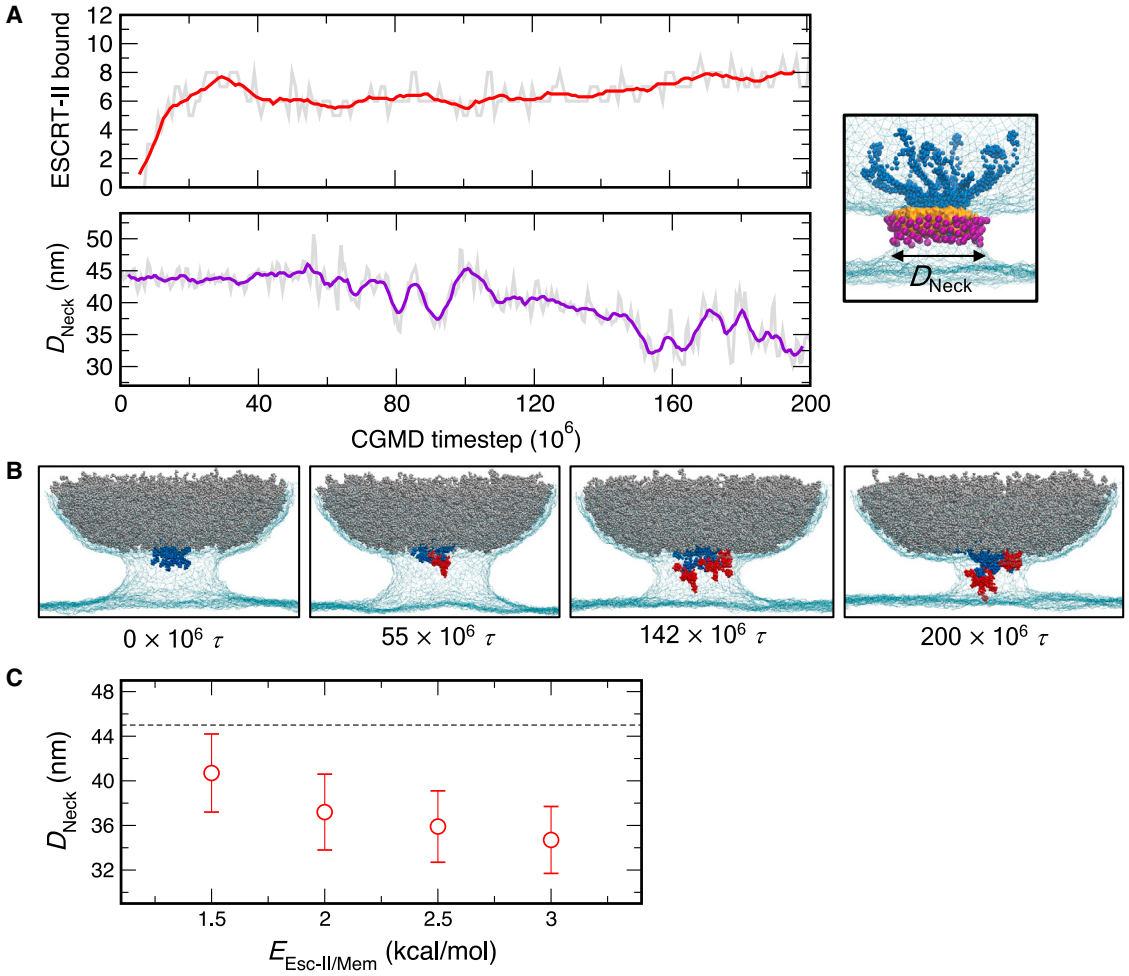

FIGURE 7 Bud neck constriction dynamics. (*A*) Time series profile of ESCRT-II recruitment is shown in solid red line (*upper panel*). Time series profile of the width of the inner edge of the bud neck (D_{Neck}) is shown as a solid purple line (*lower panel*). The solid lines are the running average calculated over 10×10^6 timesteps (*upper panel*) and 5×10^6 timesteps (*lower panel*). The shaded background is the raw data. The process depicted in the time series profile is also shown in Video S1. The snapshot depicts the region of the bud neck (shown in *purple spheres*) considered to calculate D_{Neck} overlaid on the time-averaged density of CG sites of ESCRT-II involved in lipid binding and ESCRT-I association shown in orange. Gag is not shown for clarity. (*B*) Snapshots of the bud neck at different times in the trajectory. Gag, ESCRT-I, ESCRT-II bound to ESCRT-I ring, and lipid are shown in silver, blue, red, and cyan mesh, respectively. (*C*) D_{Neck} plotted as a function of the protein-membrane interaction ($E_{Esc-II/Mem}$). The horizontal dotted line (45 nm) represents the initial diameter of the bud neck before localization of ESCRT-II at the interface of bud neck and immature Gag lattice. The error bars are calculated from final 50×10^6 CG MD timesteps. To see this figure in color, go online.

supercomplexes constrict the inner edge of the bud neck, enforcing a narrowing cone shape of the bud neck.

DISCUSSION

In this work, we elucidate the dynamical mechanisms by which multiprotein upstream ESCRT complexes are formed templated by immature Gag lattice at the edge of a budding virion. We first systematically derive bottom-up CG model and interactions between different ESCRT components and lipid from experimental structural data and extensive AA reference simulations. Using these bottom-up CG models, we simulated ESCRT-I self-assembly dynamics templated by immature Gag lattice in the absence and presence of ESCRT-II. We find that higher-order ESCRT-I oligomerization approaching the 12-membered ring is facilitated by the optimal dimension (~50 nm) of the Gag lumen. The optimal dimension of the Gag lumen corresponds to the diameter of outward projecting Gag-binding UEV domains of the ESCRT-I ring. We then simulated ESCRT-I self-assembly in the presence of ESCRT-II to examine the assembly dynamics in a realistic crowded bud neck environment where multiple upstream ESCRT components are simultaneously present. Our results demonstrate that ESCRT-I assembly competence is only slightly hindered when multiple copies of ESCRT-II crowd the bud neck. Our results demonstrate that ESCRT-I oligomerization and ESCRT-I/II supercomplex formation can occur sequentially, or it is plausible that ESCRT-I can also successfully oligomerize when both ESCRT-I and -II colocalize at the bud neck.

Importantly, we find that successful self-assembly of ESCRT-I in the presence of ESCRT-II at the bud neck is implicitly contingent on the weak interaction strength of ESCRT-I/II association. In simulations with enhanced ESCRT-I/II association strength, self-assembly of ESCRT-I to higher-order oligomers is disfavored. This can likely be attributed to extended lifetimes of the misoriented subpopulation of ESCRT-I/II supercomplexes that are detrimental to the self-assembly of ESCRT-I due to crowding of the Gag lumen. Weak interaction between ESCRT-I/II can promote frequent binding and unbinding, allowing the reorganization of ESCRT-I/II supercomplexes. Specifically, rapid dissociation of misoriented ESCRT-I/II supercomplex structures in which the VPS25 subunits are oriented toward the interior of the Gag lumen can contribute to relieving protein crowding and facilitate ESCRT-I self-assembly dynamics. To summarize, the results of this work provide important dynamical insight into the factors that regulate ESCRT-I self-assembly in a multicomponent crowded environment of a budding virion. The upstream ESCRT machinery also consists of ALIX, which binds to Gag through interactions at p6 and NC domain mediated via RNA (104,105). Therefore, during HIV-1 release, both ESCRT-I and ALIX can colocalize at the Gag lumen creating a crowded environment. How the network of interactions between different components and protein crowding regulates ESCRT-I self-assembly in the presence of ALIX, and to what extent dynamics of ESCRT-I self-assembly in the presence of ESCRT-II and ALIX are comparable can be an interesting future direction of study.

The structure of upstream ESCRT supercomplexes formed at the bud neck can shed light on how these supercomplexes orchestrate the recruitment and nucleation of ESCRT-III components. Specifically, two VPS25 subunit C-terminal tips of ESCRT-II are responsible for recruiting downstream ESCRT-III components. Our simulations indicate that ESCRT-I/II supercomplexes are predominantly oriented as column-like structures at the bud neck, with ESCRT-II spanning between the ESCRT-I headpiece ring to the outer edge of the bud neck. The column-like structures of ESCRT-I/II supercomplexes observed in our simulations at the bud neck are analogous to the crescent-like shape of the ESCRT-I/II supercomplexes observed in the solution (106). In both cases, the VPS25 tip pointed away from the ESCRT-I/II binding interfaces (i.e., $D_{\text{E1-VPS25}}$ is positive). Qualitative estimation of the structural ensemble of the ESCRT-I/II supercomplexes reveals a higher propensity of closed structures (i.e., $D_{\text{E1-VPS25}}$ negative) in solution compared with at the bud neck. This difference in behavior can be rationalized by considering that the structure of ESCRT-I/II supercomplexes at the bud neck is likely templated by the shape of virion neck during viral budding. Furthermore, the spatially confined environment of the virion bud neck likely allows limited rotational and diffusional flexibility for the ESCRT-I/II supercomplexes to adopt alternate states.

The shape of these ESCRT-I/II supercomplex structures observed in our simulations is similar to the vertical assemblies visualized by electron microscopy at the site of the Gag immature lattice (51,94). These vertical assemblies were assigned to be upstream ESCRT complexes connecting Gag lattice and ESCRT-III spirals. The structure of ESCRT-I/II supercomplexes observed at the site of Gag assembly in our simulations, therefore, provide a molecular view of these images. The structure of ESCRT-I/II supercomplexes formed in our simulations also offers important molecular insight into where at the bud neck ESCRT-III is nucleated, inferred from the spatial distribution of VPS25 subunits. In these column-like structures, VPS25 subunits are distributed in the vicinity of the outer edge of the bud neck distal to the immature Gag lattice. Based on the distribution of VPS25 subunits at the bud neck observed in our simulations, we propose the following scenario for ESCRT-III nucleation and growth at the viral budding site. In the column-like structures of ESCRT-I/II supercomplexes predominantly observed in our simulations, VPS25 subunits distributed at the outer edge of the bud neck are most likely to be accessible for association with CHMP6. Association of CHMP6 to VPS25 will also pin ESCRT-II at both ends distal and proximal to immature Gag lattice and therefore scaffolding the whole bud neck. These VPS25:(CHMP6) complexes distributed at the outer edge of the bud neck can then act as seeds for nucleation of ESCRT-III protofilaments (41). When nucleated from the outer edge of the bud neck, the ESCRT-III polymers are likely to initially grow as cone-shaped morphologies propagating outward from the bud neck to the flat section of the membrane surrounding the viral budding site (16).

Our simulations demonstrate that higher-order ESCRT-I oligomers bound to the Gag lattice act as a scaffold upon which multiple copies of ESCRT-II can bind to form ESCRT-I/II supercomplexes. Interestingly, we find that the formation of ESCRT-I/II supercomplexes initiates bud neck constriction by pulling the inner edge of the bud neck toward the outer rim of the ESCRT-I headpiece ring. We note that the diameter of the outer edge of the ESCRT-I headpiece is 17 nm. The initial bud neck diameter in our budding virion construct is 45 nm, approaching the diameter of the optimal Gag lumen (50 nm) required for ESCRT-I oligomerization. In our simulations, final diameter of the bud neck (33 nm) after several copies of ESCRT-II bind to ESCRT-I is intermediate between the dimensions of the initial bud neck and the outer rim of the ESCRT-I ring. Dimension of the constricted bud neck subsequent to the formation of the upstream ESCRT complexes is also significantly closer to the typical dimension (24 nm) of assembled ESCRT-III morphologies (16). We find that stronger ESCRT-II-membrane interactions are key to stabilizing a highly constricted bud neck. Moreover, the

constricted bud neck observed in our simulations can scaffold typical ESCRT-III polymer morphologies such as cones and tubes. Our results, therefore, demonstrate that upstream ESCRT complexes at the bud neck not only bridge the Gag lattice to downstream ESCRT-III but also modulate the membrane neck shape creating optimal circumstances for ESCRT-III nucleation and growth.

We now aim to provide an outline of which results reported in this work can be directly validated through experiments. A key aim of this work was to provide a composite molecular model of the upstream ESCRT organization templated by the immature Gag lattice. The column-like ESCRT-I/II structures observed in our CG MD simulations can be directly validated by the in vitro reconstitution and structural determination of the immature Gag and upstream ESCRT complexes by cryoelectron tomography combined with image processing using subtomogram averaging (107). The strength of the ESCRT-membrane interactions is another parameter that we modulate in our simulations to assess the modulation of bud neck dimension. Experimentally, effective protein-membrane interactions can be tuned by systematically varying the membrane composition with anionic lipids. Finally, in our simulations, we also assess how modulating the ESCRT-I/II interactions impact the ESCRT-I oligomerization dynamics. We found that stronger ESCRT-I/II interactions impeded extended ESCRT-I oligomerization. The 12-mer ESCRT-I ring bound to the immature Gag lattice acts as a nucleating platform for other upstream ESCRT and downstream ESCRT-III factors. We anticipate that the presence of smaller ESCRT-I oligomers can adversely impact all the downstream processes inhibiting scission and leading to arrested virion formation. Therefore, the results of our CG simulations can be experimentally validated by performing targeted mutations of key residues at the ESCRT-I/II binding interface and then estimating the spatial distribution of ESCRT oligomers at the budding site of arrested virions.

To summarize, in this work, we elucidated the dynamics of upstream ESCRT organization at the viral budding site. Our findings provide key molecular insight into how upstream ESCRTs can orchestrate ESCRT-III nucleation and growth at the viral budding site. First, based on the structure of ESCRT-I/II supercomplexes bound to the immature Gag lattice, we predict that ESCRT-III filaments are most likely to be nucleated from the outer edge of the bud neck distal to the Gag lattice and grow outward from the periphery of the neck into polymeric filaments. Second, we find that the ESCRT-I/II supercomplex modulates membrane shape, initiating bud neck constriction. As the membrane neck narrows, conditions become more favorable for rapid ESCRT-III recruitment and nucleation. In other words, we hypothesize that a key role of upstream ESCRT machinery is to lower the energetic barrier for ESCRT-III nucleation at the viral budding site. We expect the mechanistic insights reported here will also be broadly applicable to cellular processes other than viral budding involving the ESCRT machinery. The molecular insights revealed in this work present multiple directions of future work pertaining to how upstream ESCRT complexes mediate nucleation of ESCRT-III spirals and subsequent maturation of these spiral filaments to heteropolymeric structures that constrict the bud neck. The recently released high-resolution structure of ESCRT-III polymers is of particular relevance to investigating the budding and reverse-topology membrane scission mechanism of immature HIV-1 virions (108). Specifically, the structure of the CHMP2-CHMP3 heteropolymer reported in (108) scaffolds negatively curved membrane necks with diameters less than 45 nm, comparable with neck dimensions relevant to late-stage budding virion. Therefore, our future research efforts will focus on developing bottom-up CG models of ESCRT-III from the recently released structures of ESCRT-III heteropolymers.

DATA AVAILABILITY

The CG models of the Gag, ESCRT-I, ESCRT-II, and CG lipid, and analysis codes are available in the Github repository (https://github.com/arpahudait/Gag-ESCRT_budding). Additional details are provided within the article or supporting material. Additional data are available upon request to the author.

SUPPORTING MATERIAL

Supporting material can be found online at https://doi.org/10.1016/j.bpj.2023.05.020.

AUTHOR CONTRIBUTIONS

A.H., J.H.H., and G.A.V. designed the research. A.H. built systems, performed simulations, analyzed data, created figures, and prepared the initial manuscript draft. All authors contributed to the writing and editing of the final manuscript.

ACKNOWLEDGMENTS

The computational resources used in this work were provided by the Research Computing Center (RCC) at The University of Chicago and the Texas Advanced Computing Center (TACC) at The University of Texas at Austin. Simulations were performed using resources provided by Extreme Science and Engineering Discovery Environment (XSEDE) (109), supported by the National Science Foundation grant no. ACI-1548562, and Frontera (at TACC) funded by the NSF (OAC-1818253).

This research was supported by the National Institute of Allergy and Infectious Diseases (NIAID) of the National Institutes of Health by grants U54 AI170855 for the Behavior of HIV in Viral Environments (B-HIVE) Center (to A.H. and G.A.V.), grant P50 AI150464 for the Center for the Structural Biology of Cellular Host Elements in Egress, Trafficking, and Assembly of HIV (CHEETAH) Center (to A.H. and G.A.V.), and R37-AI112442 (to J.H.H.).

DECLARATION OF INTERESTS

J.H.H. is a co-founder and shareholder of Casma Therapeutics and receives research funding from Casma Therapeutics, Genentech, and Hoffmann-La Roche.

REFERENCES

1. Sundquist, W. I., and H. G. Kräusslich. 2012. HIV-1 assembly, budding, and maturation. *Cold Spring Harb. Perspect. Med.* 2:a006924.
2. Hurley, J. H., and A. K. Cada. 2018. Inside job: how the ESCRTs release HIV-1 from infected cells. *Biochem. Soc. Trans.* 46:1029–1036.
3. Freed, E. O. 2015. HIV-1 assembly, release and maturation. *Nat. Rev. Microbiol.* 13:484–496.
4. Briggs, J. A. G., and H. G. Kräusslich. 2011. The molecular architecture of HIV. *J. Mol. Biol.* 410:491–500.
5. Jouvenet, N., M. Zhadina, …, S. M. Simon. 2011. Dynamics of ESCRT protein recruitment during retroviral assembly. *Nat. Cell Biol.* 13:394–401.
6. Baumgärtel, V., S. Ivanchenko, …, D. C. Lamb. 2011. Live-cell visualization of dynamics of HIV budding site interactions with an ESCRT component. *Nat. Cell Biol.* 13:469–474.
7. Van Engelenburg, S. B., G. Shtengel, …, J. Lippincott-Schwartz. 2014. Distribution of ESCRT machinery at HIV assembly sites reveals virus scaffolding of ESCRT subunits. *Science.* 343:653–656.
8. Lippincott-Schwartz, J., E. O. Freed, and S. B. van Engelenburg. 2017. A consensus view of ESCRT-mediated human immunodeficiency virus type 1 abscission. *Annu. Rev. Virol.* 4:309–325.
9. Huang, M., J. M. Orenstein, …, E. O. Freed. 1995. p6Gag is required for particle production from full-length human immunodeficiency virus type 1 molecular clones expressing protease. *J. Virol.* 69:6810–6818.
10. Martin-Serrano, J., T. Zang, and P. D. Bieniasz. 2001. HIV-1 and Ebola virus encode small peptide motifs that recruit Tsg101 to sites of particle assembly to facilitate egress. *Nat. Med.* 7:1313–1319.
11. Garrus, J. E., U. K. von Schwedler, …, W. I. Sundquist. 2001. Tsg101 and the vacuolar protein sorting pathway are essential for HIV-1 budding. *Cell.* 107:55–65.
12. Demirov, D. G., A. Ono, …, E. O. Freed. 2002. Overexpression of the N-terminal domain of TSG101 inhibits HIV-1 budding by blocking late domain function. *Proc. Natl. Acad. Sci. USA.* 99:955–960.
13. Wollert, T., and J. H. Hurley. 2010. Molecular mechanism of multivesicular body biogenesis by ESCRT complexes. *Nature.* 464:864–869.
14. Vietri, M., K. O. Schink, …, H. Stenmark. 2015. Spastin and ESCRT-III coordinate mitotic spindle disassembly and nuclear envelope sealing. *Nature.* 522:231–235.
15. Elia, N., R. Sougrat, …, J. Lippincott-Schwartz. 2011. Dynamics of endosomal sorting complex required for transport (ESCRT) machinery during cytokinesis and its role in abscission. *Proc. Natl. Acad. Sci. USA.* 108:4846–4851.
16. McCullough, J., A. K. Clippinger, …, A. Frost. 2015. Structure and membrane remodeling activity of ESCRT-III helical polymers. *Science.* 350:1548–1551.
17. Bertin, A., N. de Franceschi, …, P. Bassereau. 2020. Human ESCRT-III polymers assemble on positively curved membranes and induce helical membrane tube formation. *Nat. Commun.* 11:2663.
18. Cada, A. K., M. R. Pavlin, …, J. H. Hurley. 2022. Friction-driven membrane scission by the human ESCRT-III proteins CHMP1B and IST1. *Proc. Natl. Acad. Sci. USA.* 119:e2204536119.
19. Bleck, M., M. S. Itano, …, S. M. Simon. 2014. Temporal and spatial organization of ESCRT protein recruitment during HIV-1 budding. *Proc. Natl. Acad. Sci. USA.* 111:12211–12216.
20. Dick, R. A., and V. M. Vogt. 2014. Membrane interaction of retroviral Gag proteins. *Front. Microbiol.* 5:187.
21. Monje-Galvan, V., and G. A. Voth. 2020. Binding mechanism of the matrix domain of HIV-1 gag on lipid membranes. *Elife.* 9, e58621.
22. Schur, F. K. M., W. J. H. Hagen, …, J. A. G. Briggs. 2015. Structure of the immature HIV-1 capsid in intact virus particles at 8.8 Å resolution. *Nature.* 517:505–508.
23. Bharat, T. A. M., L. R. Castillo Menendez, …, J. A. G. Briggs. 2014. Cryo-electron microscopy of tubular arrays of HIV-1 Gag resolves structures essential for immature virus assembly. *Proc. Natl. Acad. Sci. USA.* 111:8233–8238.
24. Bayro, M. J., B. K. Ganser-Pornillos, …, R. Tycko. 2016. Helical conformation in the CA-SP1 junction of the immature HIV-1 lattice determined from solid-state NMR of virus-like particles. *J. Am. Chem. Soc.* 138:12029–12032.
25. Carlson, L.-A., A. de Marco, …, K. Grünewald. 2010. Cryo electron tomography of native HIV-1 budding sites. *PLoS Pathog.* 6, e1001173.
26. Wright, E. R., J. B. Schooler, …, G. J. Jensen. 2007. Electron cryotomography of immature HIV-1 virions reveals the structure of the CA and SP1 Gag shells. *EMBO J.* 26:2218–2226.
27. Carlson, L.-A., J. A. G. Briggs, …, H. G. Kräusslich. 2008. Three-dimensional analysis of budding sites and released virus suggests a revised model for HIV-1 morphogenesis. *Cell Host Microbe.* 4:592–599.
28. Carlson, L.-A., and J. H. Hurley. 2012. In vitro reconstitution of the ordered assembly of the endosomal sorting complex required for transport at membrane-bound HIV-1 Gag clusters. *Proc. Natl. Acad. Sci. USA.* 109:16928–16933.
29. VerPlank, L., F. Bouamr, …, C. A. Carter. 2001. Tsg101, a homologue of ubiquitin-conjugating (E2) enzymes, binds the L domain in HIV type 1 Pr55Gag. *Proc. Natl. Acad. Sci. USA.* 98:7724–7729.
30. Im, Y. J., L. Kuo, …, J. H. Hurley. 2010. Crystallographic and functional analysis of the ESCRT-I/HIV-1 gag PTAP interaction. *Structure.* 18:1536–1547.
31. Pornillos, O., S. L. Alam, …, W. I. Sundquist. 2002. Structure of the Tsg101 UEV domain in complex with the PTAP motif of the HIV-1 p6 protein. *Nat. Struct. Biol.* 9:812–817.
32. Strack, B., A. Calistri, …, H. G. Göttlinger. 2003. AIP1/ALIX is a binding partner for HIV-1 p6 and EIAV p9 functioning in virus budding. *Cell.* 114:689–699.
33. Fisher, R. D., H.-Y. Chung, …, C. P. Hill. 2007. Structural and biochemical studies of ALIX/AIP1 and its role in retrovirus budding. *Cell.* 128:841–852.
34. Munshi, U. M., J. Kim, …, E. O. Freed. 2007. An alix fragment potently inhibits HIV-1 budding: characterization of binding to retroviral YPXL late domains. *J. Biol. Chem.* 282:3847–3855.
35. Zhai, Q., R. D. Fisher, …, C. P. Hill. 2008. Structural and functional studies of ALIX interactions with YPXnL late domains of HIV-1 and EIAV. *Nat. Struct. Mol. Biol.* 15:43–49.
36. Flower, T. G., Y. Takahashi, …, J. H. Hurley. 2020. A helical assembly of human ESCRT-I scaffolds reverse-topology membrane scission. *Nat. Struct. Mol. Biol.* 27:570–580.
37. Im, Y. J., and J. H. Hurley. 2008. Integrated structural model and membrane targeting mechanism of the human ESCRT-II complex. *Dev. Cell.* 14:902–913.
38. Langelier, C., U. K. von Schwedler, …, W. I. Sundquist. 2006. Human ESCRT-II complex and its role in human immunodeficiency virus type 1 release. *J. Virol.* 80:9465–9480.
39. Im, Y. J., T. Wollert, …, J. H. Hurley. 2009. Structure and function of the ESCRT-II-III interface in multivesicular body biogenesis. *Dev. Cell.* 17:234–243.
40. Yorikawa, C., H. Shibata, …, M. Maki. 2005. Human CHMP6, a myristoylated ESCRT-III protein, interacts directly with an ESCRT-II component EAP20 and regulates endosomal cargo sorting. *Biochem. J.* 387:17–26.
41. Lee, I.-H., H. Kai, …, J. H. Hurley. 2015. Negative membrane curvature catalyzes nucleation of endosomal sorting complex required for transport (ESCRT)-III assembly. *Proc. Natl. Acad. Sci. USA.* 112:15892–15897.
42. Prescher, J., V. Baumgärtel, …, D. C. Lamb. 2015. Super-resolution imaging of ESCRT-proteins at HIV-1 assembly sites. *PLoS Pathog.* 11, e1004677.

43. Meng, B., N. C. Y. Ip, …, A. M. L. Lever. 2015. Evidence that the endosomal sorting complex required for transport-II (ESCRT-II) is required for efficient human immunodeficiency virus-1 (HIV-1) production. *Retrovirology.* 12:72.

44. Meng, B., N. C. Y. Ip, …, A. M. L. Lever. 2020. ESCRT-II functions by linking to ESCRT-I in human immunodeficiency virus-1 budding. *Cell Microbiol.* 22, e13161.

45. Mercredi, P. Y., N. Bucca, …, M. F. Summers. 2016. Structural and molecular determinants of membrane binding by the HIV-1 matrix protein. *J. Mol. Biol.* 428:1637–1655.

46. Favard, C., J. Chojnacki, …, D. Muriaux. 2019. HIV-1 Gag specifically restricts PI(4,5)P2 and cholesterol mobility in living cells creating a nanodomain platform for virus assembly. *Sci. Adv.* 5, eaaw8651.

47. Yandrapalli, N., Q. Lubart, …, C. Favard. 2016. Self assembly of HIV-1 Gag protein on lipid membranes generates PI(4,5)P2/Cholesterol nanoclusters. *Sci. Rep.* 6, 39332.

48. Mücksch, F., V. Laketa, …, H. G. Kräusslich. 2017. Synchronized HIV assembly by tunable PIP2 changes reveals PIP2 requirement for stable Gag anchoring. *Elife.* 6, e25287.

49. Chiaruttini, N., L. Redondo-Morata, …, A. Roux. 2015. Relaxation of loaded ESCRT-III spiral springs drives membrane deformation. *Cell.* 163:866–879.

50. Hanson, P. I., R. Roth, …, J. E. Heuser. 2008. Plasma membrane deformation by circular arrays of ESCRT-III protein filaments. *J. Cell Biol.* 180:389–402.

51. Cashikar, A. G., S. Shim, …, P. I. Hanson. 2014. Structure of cellular ESCRT-III spirals and their relationship to HIV budding. *Elife.* 3, e02184.

52. Effantin, G., A. Dordor, …, W. Weissenhorn. 2013. ESCRT-III CHMP2A and CHMP3 form variable helical polymers in vitro and act synergistically during HIV-1 budding. *Cell Microbiol.* 15:213–226.

53. Lata, S., G. Schoehn, …, W. Weissenhorn. 2008. Helical structures of ESCRT-III are disassembled by VPS4. *Science.* 321:1354–1357.

54. Agudo-Canalejo, J., and R. Lipowsky. 2018. Domes and cones: adhesion-induced fission of membranes by ESCRT proteins. *PLoS Comput. Biol.* 14, e1006422.

55. Harker-Kirschneck, L., B. Baum, and A. E. Šarić. 2019. Changes in ESCRT-III filament geometry drive membrane remodelling and fission in silico. *BMC Biol.* 17:82.

56. Liese, S., E. M. Wenzel, …, A. Carlson. 2020. Protein crowding mediates membrane remodeling in upstream ESCRT-induced formation of intraluminal vesicles. *Proc. Natl. Acad. Sci. USA.* 117:28614–28624.

57. Snead, W. T., C. C. Hayden, …, J. C. Stachowiak. 2017. Membrane fission by protein crowding. *Proc. Natl. Acad. Sci. USA.* 114:E3258–E3267.

58. Mercker, M., and A. Marciniak-Czochra. 2015. Bud-neck scaffolding as a possible driving force in ESCRT-induced membrane budding. *Biophys. J.* 108:833–843.

59. Różycki, B., E. Boura, …, G. Hummer. 2012. Membrane-elasticity model of coatless vesicle budding induced by ESCRT complexes. *PLoS Comput. Biol.* 8, e1002736.

60. Pak, A. J., J. M. A. Grime, …, G. A. Voth. 2017. Immature HIV-1 lattice assembly dynamics are regulated by scaffolding from nucleic acid and the plasma membrane. *Proc. Natl. Acad. Sci. USA.* 114:E10056–E10065.

61. Jin, J., A. J. Pak, …, G. A. Voth. 2022. Bottom-up coarse-graining: principles and perspectives. *J. Chem. Theory Comput.* 18:5759–5791.

62. Alam, S. L., C. Langelier, …, W. I. Sundquist. 2006. Structural basis for ubiquitin recognition by the human ESCRT-II EAP45 GLUE domain. *Nat. Struct. Mol. Biol.* 13:1029–1030.

63. Song, Y., F. DiMaio, …, D. Baker. 2013. High-resolution comparative modeling with RosettaCM. *Structure.* 21:1735–1742.

64. Yang, J., I. Anishchenko, …, D. Baker. 2020. Improved protein structure prediction using predicted interresidue orientations. *Proc. Natl. Acad. Sci. USA.* 117:1496–1503.

65. Jo, S., T. Kim, …, W. Im. 2008. CHARMM-GUI: a web-based graphical user interface for CHARMM. *J. Comput. Chem.* 29:1859–1865.

66. Evans, D. J., and B. L. Holian. 1985. The nose–Hoover thermostat. *J. Chem. Phys.* 83:4069–4074.

67. Parrinello, M., and A. Rahman. 1981. Polymorphic transitions in single crystals: a new molecular dynamics method. *J. Appl. Phys.* 52:7182–7190.

68. Huang, J., S. Rauscher, …, A. D. MacKerell. 2017. CHARMM36m: an improved force field for folded and intrinsically disordered proteins. *Nat. Methods.* 14:71–73.

69. Jorgensen, W. L., J. Chandrasekhar, …, M. L. Klein. 1983. Comparison of simple potential functions for simulating liquid water. *J. Chem. Phys.* 79:926–935.

70. Hess, B., H. Bekker, J. G. M. Fraaije…, 1997. LINCS: a linear constraint solver for molecular simulations. *J. Comput. Chem.* 18:1463–1472.

71. Darden, T., D. York, and L. Pedersen. 1993. Particle mesh Ewald: an N•log(N) method for Ewald sums in large systems. *J. Chem. Phys.* 98:10089–10092.

72. Abraham, M. J., T. Murtola, …, E. Lindahl. 2015. GROMACS: high performance molecular simulations through multi-level parallelism from laptops to supercomputers. *SoftwareX.* 1-2:19–25.

73. Kumar, S., J. M. Rosenberg, …, P. A. Kollman. 1992. THE weighted histogram analysis method for free-energy calculations on biomolecules. I. The method. *J. Comput. Chem.* 13:1011–1021.

74. Souaille, M., and B. Roux. 2001. Extension to the weighted histogram analysis method: combining umbrella sampling with free energy calculations. *Comput. Phys. Commun.* 135:40–57.

75. Zhu, F., and G. Hummer. 2012. Convergence and error estimation in free energy calculations using the weighted histogram analysis method. *J. Comput. Chem.* 33:453–465.

76. Zhang, Z., L. Lu, …, G. A. Voth. 2008. A systematic methodology for defining coarse-grained sites in large biomolecules. *Biophys. J.* 95:5073–5083.

77. Lyman, E., J. Pfaendtner, and G. A. Voth. 2008. Systematic multiscale parameterization of heterogeneous elastic network models of proteins. *Biophys. J.* 95:4183–4192.

78. Grime, J. M. A., and J. J. Madsen. 2019. Efficient simulation of tunable lipid assemblies across scales and resolutions. Preprint at arXiv 1910.05362. https://doi.org/10.48550/arXiv.1910.05362.

79. Shell, M. S. 2008. The relative entropy is fundamental to multiscale and inverse thermodynamic problems. *J. Chem. Phys.* 129, 144108.

80. Yu, A., A. J. Pak, …, G. A. Voth. 2021. A multiscale coarse-grained model of the SARS-CoV-2 virion. *Biophys. J.* 120:1097–1104.

81. Pak, A. J., A. Yu, …, G. A. Voth. 2022. Cooperative multivalent receptor binding promotes exposure of the SARS-CoV-2 fusion machinery core. *Nat. Commun.* 13:1002.

82. Beutler, T. C., A. E. Mark, …, W. F. van Gunsteren. 1994. Avoiding singularities and numerical instabilities in free energy calculations based on molecular simulations. *Chem. Phys. Lett.* 222:529–539.

83. Plimpton, S. 1995. Fast parallel algorithms for short-range molecular dynamics. *J. Comput. Phys.* 117:1–19.

84. Tribello, G. A., M. Bonomi, …, G. Bussi. 2014. Plumed 2: new feathers for an old bird. *Comput. Phys. Commun.* 185:604–613.

85. Martyna, G. J., D. J. Tobias, and M. L. Klein. 1994. Constant pressure molecular dynamics algorithms. *J. Chem. Phys.* 101:4177–4189.

86. Schneider, T., and E. Stoll. 1978. Molecular-dynamics study of a three-dimensional one-component model for distortive phase transitions. *Phys. Rev. B.* 17:1302–1322.

87. Tribello, G. A., F. Giberti, …, M. Parrinello. 2017. Analyzing and driving cluster formation in atomistic simulations. *J. Chem. Theory Comput.* 13:1317–1327.

88. Angioletti-Uberti, S., M. Ceriotti, …, M. W. Finnis. 2010. Solid-liquid interface free energy through metadynamics simulations. *Phys. Rev. B.* 81, 125416.

89. Cheng, B., G. A. Tribello, and M. Ceriotti. 2015. Solid-liquid interfacial free energy out of equilibrium. *Phys. Rev. B.* 92, 180102.

90. Hierro, A., J. Sun, …, J. H. Hurley. 2004. Structure of the ESCRT-II endosomal trafficking complex. *Nature.* 431:221–225.

91. Saunders, M. G., and G. A. Voth. 2013. Coarse-graining methods for computational biology. *Annu. Rev. Biophys.* 42:73–93.

92. Evans, R., M. O'Neill, …, D. Hassabis. 2022. Protein complex prediction with AlphaFold-Multimer. Preprint at bioRxiv. https://doi.org/10.1101/2021.10.04.463034.

93. Boura, E., V. Ivanov, …, J. H. Hurley. 2012. Endosomal sorting complex required for transport (ESCRT) complexes induce phase-separated microdomains in supported lipid bilayers. *J. Biol. Chem.* 287:28144–28151.

94. Ladinsky, M. S., C. Kieffer, …, P. J. Bjorkman. 2014. Electron tomography of HIV-1 infection in gut-associated lymphoid tissue. *PLoS Pathog.* 10, e1003899.

95. Barducci, A., G. Bussi, and M. Parrinello. 2008. Well-tempered metadynamics: a smoothly converging and tunable free-energy method. *Phys. Rev. Lett.* 100, 020603.

96. Dama, J. F., M. Parrinello, and G. A. Voth. 2014. Well-tempered metadynamics converges asymptotically. *Phys. Rev. Lett.* 112, 240602.

97. Bonomi, M., A. Barducci, and M. Parrinello. 2009. Reconstructing the equilibrium Boltzmann distribution from well-tempered metadynamics. *J. Comput. Chem.* 30:1615–1621.

98. Tiwary, P., and M. Parrinello. 2015. A time-independent free energy estimator for metadynamics. *J. Phys. Chem. B.* 119:736–742.

99. Blood, P. D., and G. A. Voth. 2006. Direct observation of Bin/amphiphysin/Rvs (BAR) domain-induced membrane curvature by means of molecular dynamics simulations. *Proc. Natl. Acad. Sci. USA.* 103:15068–15072.

100. Simunovic, M., E. Evergren, …, P. Bassereau. 2016. How curvature-generating proteins build scaffolds on membrane nanotubes. *Proc. Natl. Acad. Sci. USA.* 113:11226–11231.

101. Ford, M. G. J., I. G. Mills, …, H. T. McMahon. 2002. Curvature of clathrin-coated pits driven by epsin. *Nature.* 419:361–366.

102. Schmidt, N. W., A. Mishra, …, G. C. L. Wong. 2013. Influenza virus A M2 protein generates negative Gaussian membrane curvature necessary for budding and scission. *J. Am. Chem. Soc.* 135:13710–13719.

103. Stachowiak, J. C., C. C. Hayden, and D. Y. Sasaki. 2010. Steric confinement of proteins on lipid membranes can drive curvature and tubulation. *Proc. Natl. Acad. Sci. USA.* 107:7781–7786.

104. Lee, S., A. Joshi, …, J. H. Hurley. 2007. Structural basis for viral late-domain binding to Alix. *Nat. Struct. Mol. Biol.* 14:194–199.

105. Sette, P., V. Dussupt, and F. Bouamr. 2012. Identification of the HIV-1 NC binding interface in alix Bro1 reveals a role for RNA. *J. Virol.* 86:11608–11615.

106. Boura, E., B. Różycki, …, G. Hummer. 2012. Solution structure of the ESCRT-I and -ii supercomplex: implications for membrane budding and scission. *Structure.* 20:874–886.

107. Briggs, J. A. G. 2013. Structural biology in situ—the potential of subtomogram averaging. *Curr. Opin. Struct. Biol.* 23:261–267.

108. Azad, K., D. Guilligay, …, W. Weissenhorn. 2023. Structural basis of CHMP2A–CHMP3 ESCRT-III polymer assembly and membrane cleavage. *Nat. Struct. Mol. Biol.* 30:81–90.

109. Towns, J., T. Cockerill, …, N. Wilkins-Diehr. 2014. XSEDE: accelerating scientific Discovery. *Comput. Sci. Eng.* 16:62–74.